

DESIGN, SPECIFICATION, AND PRODUCTION OF AN F/2 BROADBAND INFRARED  
HIGH PERFORMANCE OBJECTIVE LENS ASSEMBLY

by

Taylor Sorensen

---

Copyright © Taylor Sorensen 2016

A Master's Report Submitted to the Faculty of the

COLLEGE OF OPTICAL SCIENCES

In Partial Fulfillment of the Requirements

For the Degree of

MASTER OF SCIENCE

In the Graduate College

THE UNIVERSITY OF ARIZONA

2016

## ACKNOWLEDGEMENTS

I would like to thank the entire faculty and staff at the University of Arizona's College of Optical Sciences. Without their guidance and instruction, the subject material of this report would not have been possible. I would like to thank Cindy Robertson in particular for all of her efforts coordinating the Distance Learning Program. I would like to thank my Master's Committee, comprised of Dr. Michael Nofziger, Dr. James Schwiegerling, and my Master's Advisor Dr. José Sasián, all of whom I have had the pleasure of taking courses from throughout both my undergraduate and graduate career.

In addition, I would like to thank my undergraduate classmate, friend, and former Assembly Manager at II-VI Optical Systems, Sam Goldstein, for his help in getting my lens design assembled. Special thanks are also due to countless others at II-VI Optical Systems for their involvement.

Finally, I would like to thank all of the folks at Synopsys Optical Solutions Group, formerly known as Optical Research Associates, for their development and support of Code V, which I continue to use as my preferred optical design tool since I was first introduced to it in 2008 as an undergraduate student.

## Table of Contents

Abstract.....	7
INTRODUCTION .....	8
PART I: DESIGN .....	10
Getting Started .....	10
<i>Design Tools</i> .....	10
<i>Table 1</i> .....	11
<i>Starting Design</i> .....	13
<i>Cold Stop and Dewar</i> .....	14
<i>Defining Wavelength</i> .....	16
Scaling and Optimizing.....	18
Final Design and Performance.....	19
<i>Ensquared Energy</i> .....	22
<i>Distortion</i> .....	24
<i>Relative Illumination</i> .....	26
<i>Modulation Transfer Function</i> .....	27
<i>Optical Path Difference</i> .....	30
<i>Design Compliance Matrix</i> .....	32
Tolerancing.....	33
<i>Code V Reduce Tolerance Sensitivities Feature</i> .....	34
<i>Final Tolerance Set</i> .....	35
PART II: OPTICAL COMPONENT FABRICATION AND VERIFICATION .....	39
Mechanical Components.....	39
Optical Component Fabrication Methods.....	41
<i>Conventional Fabrication</i> .....	41
<i>Singe Point Diamond Turning</i> .....	42
Component Verification.....	43
<i>Mid-Spatial Frequency Error</i> .....	43
<i>Interferometric Verification of Spherical Surfaces</i> .....	44
<i>Profilometer Verification of Aspheric Surfaces</i> .....	46
<i>Surface Roughness Verification</i> .....	47
Anti-Reflection Coatings .....	48
PART III: ASSEMBLY .....	50
Assembly Methods.....	50
<i>Aft Cell</i> .....	51
<i>Forward Cell</i> .....	53
<i>Delrin Sleeve and Outer Housing</i> .....	54
PART IV: SYSTEM TEST AND FINAL AS-BUILT RESULTS.....	56
Test Setup.....	56
Performance Measurements.....	58
<i>Ensquared Energy</i> .....	60
<i>Field of View</i> .....	61
<i>Distortion</i> .....	62
<i>Relative Illumination</i> .....	63
<i>Boresight Accuracy</i> .....	63

CONCLUSION.....	66
APPENDIX A: EVOLUTION OF THE OPTICAL DESIGN .....	68
APPENDIX B: PARAXIAL RAY TRACE AND ABERRATION THEORY .....	73
APPENDIX C: TOLERANCE SENSITIVITIES.....	76

## Table of Figures

Figure 1: Lens Design Starting Point 53.6mm EFL F/2.68 .....	13
Figure 2: Cold Stop Efficiency and F/# Matching.....	15
Figure 3: Dewar and Detector Configuration .....	16
Figure 4: Blackbody Radiation from a 1000K Source.....	18
Figure 5: Layout of Final Lens Design.....	20
Figure 6: Field Definitions.....	21
Figure 7: Ensquared versus Encircled Energy .....	22
Figure 8: Encircled Energy .....	23
Figure 9: Through Focus Encircled Energy - 25micron diameter .....	24
Figure 10: Field Curves and Distortion .....	26
Figure 11: Relative Illumination.....	27
Figure 12: MTF.....	29
Figure 13: MTF (Increased Spatial Frequency).....	29
Figure 14: Through Focus MTF .....	30
Figure 15: Optical Path Difference.....	31
Figure 16: Tolerance Analysis Results - RMS Wavefront Error.....	36
Figure 17: 2-D Section View of Opto-Mechanical Assembly (Dewar Filter and Window elements not shown) .....	40
Figure 18: Element 2 – CaF2 .....	41
Figure 19: Element 5 – IG-3 .....	41
Figure 20: Element 1 Surface 1 Surface Figure Measurement without Mid-Spatial Frequency Filtering.....	45
Figure 21: Element 1 Surface 1 Surface Figure Measurement with Mid-Spatial Frequency Filtering.....	46
Figure 22: Single TalySurf Scan of an Aspheric Surface.....	47
Figure 23: Aft Cell in Kinematic Mount Tooling.....	52
Figure 24: Element 1 tack bonded into Forward Lens Cell.....	53
Figure 25: Cross Section of Mechanical Cell Mounted to Kinematic Tool .....	54
Figure 26: Exploded View of Main Mechanical Components .....	54
Figure 27: Objective Lens Assembly - Front.....	55
Figure 28: Objective Lens Assembly - Rear.....	55
Figure 29: Basic Ensquared Energy Test Bench Components .....	57
Figure 30: UUT and Detector Stage Assembly - Front .....	58
Figure 31: UUT and Detector Stage Assembly - Rear .....	58
Figure 32: Test Field Points at Image Plane .....	59
Figure 33: Through Focus Ensquared Energy Test Result .....	61
Figure 34: Field of View Test Result.....	62
Figure 35: Relative Illumination Test Result.....	63
Figure 36: Boresight Test Result .....	64
Figure 37: High Resolution Photograph of F/2 Broadband Infrared High Performance Objective Lens Assembly.....	67
Figure 38: Marginal (Red) and Chief (Blue) Rays .....	75

## Table of Tables

Table 1: Summary of Requirements .....	12
Table 2: Design Compliance Matrix.....	32
Table 3: Element Surface Radius and Irregularity Tolerances .....	37
Table 4: Element Center Thickness Tolerances.....	37
Table 5: Assembly Airspace Tolerances.....	38
Table 6: Assembly Tilt and Decenter Tolerances.....	38
Table 7: Summary of Test Results for 39 Assemblies.....	65

### Abstract

This report will discuss the complete efforts from concept design to full production of a high performance broadband SWIR fixed focal length objective lens assembly. Custom designed to meet a full set of end user specified requirements, the lens assembly images from 1.3 to 4.0 microns with low distortion and high ensquared energy over the full image format. With a 29.8mm effective focal length and 20.5mm image diagonal, the objective provides high resolution imaging over a 38 degree circular field of view. Optimized for ensquared energy, the system is ideal for signal detection applications. In addition, the lens is passively athermal over the temperature range of 0 to 40 degrees Celsius and is vented for reduced sensitivity to pressure changes induced by altitude. The final design is a six element, compact objective, although the starting point for the design had as many as eight elements and was almost 2x the required focal length. The evolution from a proof of concept to a manufacturable design will be discussed, and the performance of the final design will be presented. Considerations for component and assembly tolerances that are achievable in the shop and on the production floor are accounted for, and an assembly level test is designed. Furthermore, special consideration of the ability to test each element through common methods and with currently available equipment was made when specifying each optical element. Assembly guidelines and targets were established in order to achieve high yield and minimal rework. Final performance results representing multiple as-built assemblies will be compared against the modeled predictions, showing good agreement.

## INTRODUCTION

The first step to tackling any significant design task is to fully define and understand a complete set of requirements of what the final product should do. This sets the expectations of the customer, but more importantly it defines the scope of the designer's efforts as he explores the design space. Without this crucial first step, the designer can easily become lost as he works towards his solution. Lens design is by no means an exception to this rule. Industry leader Robert Shannon described lens design as an art. Even the most novice lens designer will certainly understand this.

In the field of infrared optical systems, there are three general sections of the electromagnetic spectrum over which most systems are designed to operate. The short wave infrared, or SWIR, ranges from around 1.0 micron to 2.0 microns by most definitions. The mid wave infrared, or MWIR, picks up where the SWIR falls off at around 3.0 microns and extends to 5.0 microns. The long wave infrared, or LWIR, extends from 8.0 microns to roughly 12.0 to 14.0 microns, or even as far as 30.0 microns depending on the application. Most infrared optical systems will operate in only one of these wavebands or even just in a subsection of one, mostly due to limitations caused by detector materials, lens materials, and the ability of a lens design to correct for chromatic aberration over large wavebands. Recently, material suppliers have been developing specialized materials with transmission and dispersive properties that would enable optical designers to create lens designs whose aberrations are corrected over wider regions of the IR wavelength range. However, many of the applications of infrared optical systems are unique to a particular waveband. For instance, the launch and propulsion of many rocket and missile systems can be sensed and viewed in the MWIR band. Ambient temperature objects, including humans, emit thermal radiation that peaks in the middle of the LWIR band. SWIR wavelengths

can penetrate through fog and other atmospheric conditions more easily than visible wavelengths, making SWIR optical systems instrumental in detection and surveillance applications. Whatever the application, designing optical systems for imaging in the infrared requires an understanding of a few subtle, yet vitally important differences between designing visible optical systems, which Robert Fischer points out in his paper, “What’s so Different About IR Lens Design?” Despite these differences that can “make the design of thermal infrared imaging systems challenging and occasionally troublesome,” states Robert, “the task is manageable and high performance systems can be designed and implemented” (1992, p. 126), as will be demonstrated here.

## PART I: DESIGN

A rather unique optical system that images from the middle of the SWIR band to the middle of the MIWR band is designed and produced to a specific set of customer requirements. The end use application of the optical system is not explicitly disclosed, although it is likely for aircraft based surveillance or detection. The customer's requirements were delivered in the form of a specification document, outlining the various optical performance requirements, operating environments, and mass and volume limits. The set of requirements is organized into a "Table 1" format. The purpose of a "Table 1" is to serve as a single reference of the driving optical requirements and to tabulate some basic optical parameters of the design using fundamental equations and rules of thumb. "Table 1" helps the designer understand what is achievable from a design up to the diffraction limits. Just like back of the envelope and first order calculations, "Table 1" is another tool in the designer's arsenal.

### **Getting Started**

#### *Design Tools*

In any design effort, it is important to determine early on which tools will be used to perform the work, and to understand the features and any limitations of those tools. Advances in software development and computing have contributed to the availability of highly robust and powerful optical design and analysis codes; many of which have origins dating back to the early 1970s, and therefore, have decades of development and improvement behind them. Code V, first offered as a leased package in 1975 by Optical Research Associates, is an example of such a code, and is revered as one of the most premier optical design and analysis suites in the industry. First run on a General Automation minicomputer, Code V continues to provide superior optimization, tolerancing, and analysis features to users today on personal computers that are

thousands of times faster (Synopsys, 2015). Standing for “Computer-aided Optical Design and Evaluation, version 5”, Code V became a commercial product with version 5, and has been trademarked and known as “Code V” ever since (D. Lieu, personal communication, February 29, 2016). Code V was used exclusively to develop, optimize, tolerance, and fully analyze the custom SWIR-MWIR objective lens assembly that is the subject of this report.

The next most crucial, and often most challenging, step of the optical design process is determining a starting point for the lens design. This step becomes easier with experience, and it is what separates a skilled lens designer from an engineer with access to an expensive optical design software package. Even the most advanced optimization algorithm will fail to converge to a proper solution without an initial starting point as an input. In many cases, the starting point of one optical design is another similar lens design. Many optical design software packages include libraries of example lens designs of the common forms and an extensive database of patented lens designs. These resources can be consulted for a lens design that has the desired basic properties like effective focal length and focal ratio to use as a baseline. Scaling an existing lens design to obtain the required focal length can also be an option, however, one must remember that all of the parameters of the design will scale as well, including spot size, aberrations, and clear apertures, to name a few.

#### *Table 1*

Before searching for a suitable starting point, all “Table 1” requirements and calculations are organized and reviewed. See Table 1 on the next page. All customer specified requirements are identified with bold text. All other parameters are either derived from specified requirements or calculated using first order relationships. In addition to performance requirements, operating and storage environments are defined in terms of temperature and altitude.

Waveband	1	2	3	4	5			
Spectral Weighting	10	86	176	203	202			
WL, nm	<b>1300</b>	2000	2800	3500	<b>3950</b>			
DL Spot Radius, um	3.2	4.9	6.9	8.6	9.7			
DL Divergence, mr	0.05328	0.08197	0.11476	0.14345	0.16190			
EFL	29.77	mm						
<b>Entrance Pupil Diameter</b>	<b>15.00</b>	mm						
<b>FNO</b>	<b>2.008</b>	Defined by Cold Stop		1.985	Defined by EFL and Entrance Pupil			
DL spot radius	6.9	um	at Waveband 3					
N.A.	0.249							
MTF Cutoff Frequency	383.1	cycles						
Pixel Size X,Y ; Nyquist lp/mm	<b>0.025</b>	<b>0.025</b>	mm	<b>20.0</b>	cycles/mm			
Pixel IFOV	0.840	mr						
Array Size	<b>640</b>	<b>512</b>						
Array Size: L,W,Diag	<b>16</b>	<b>12.8</b>	<b>20.49</b>	mm	8.0	6.4	10.245	HFOV
FFOV: Az, El, rd	0.525	0.424			Reported FOVs include effects of distortion			
FFOV: Az, El, Degrees	30.102	24.279						
FFOV: Corner, rd	0.663	HFOV	0.331	rd				
FFOV: Corner, Degrees	37.973	HFOV	18.987	Degrees				
BFL	33.05	mm						
Cold Filter	<b>0.50</b>	<b>ZnS</b>	CS - FPA dist	<b>25.501</b>	mm	CS Diameter	<b>12.7 mm</b>	
Warm Filter	<b>1.00</b>	<b>ZnS</b>						
FPA Window	<b>1.00</b>	<b>Sapphire</b>		<u>Other Requirements</u>				
OAL, max	95.0	mm	E1 S1 to E6 S2	Distortion	<b>&lt;2%</b>			
Op Temperature, C	<b>0</b>	<b>40</b>		EE	<b>&gt;70% within 25µm pixel</b>	0 to 6.4 mm Img Height		
Perf Temperature, C	<b>5</b>	<b>35</b>		EE	<b>&gt;60% within 25µm pixel</b>	at 10.245 mm Img Height		
Store Temperature, C	<b>-40</b>	<b>70</b>		Reltv Illm	<b>≥70% at corners</b>			
Op Pressure, Altitude, kft	<b>0</b>	<b>10</b>		Avg Trans	<b>&gt;81% from 2.9-3.95µm and &gt;50% from 1.3-2.8µm</b>			
Op Pressure, PSI	<b>14.7</b>	<b>10.1</b>		Boresight	<b>&lt;100 µm displ btw optical and mech axes</b>			
				Jitter	<b>&lt;10 µm displ</b>			

Table 1: Summary of Requirements

### *Starting Design*

The starting point of this design was a previously proposed lens prescription with a total of 8 elements and an effective focal length of 53.6mm. Operating at F/2.68, this lens was characterized by a well-corrected image on a flat plane over a fairly broad spectrum of 1.3 – 4.2 microns. The small amount of chromatic aberration over a waveband similar to the waveband in the Table 1 Requirements made this lens appealing as a possible starting point. Another interesting characteristic of this existing 53.6mm efl lens was its unique combination of optical materials, including 6 zinc selenide elements, and 2 elements made from IG-3 and IG-5, which are specialty chalcogenide glasses developed by Schott Advanced Optics. Figure 1 shows a 2-dimensional layout of the starting design, with the center, upper, and lower rim rays traced for three different field points.

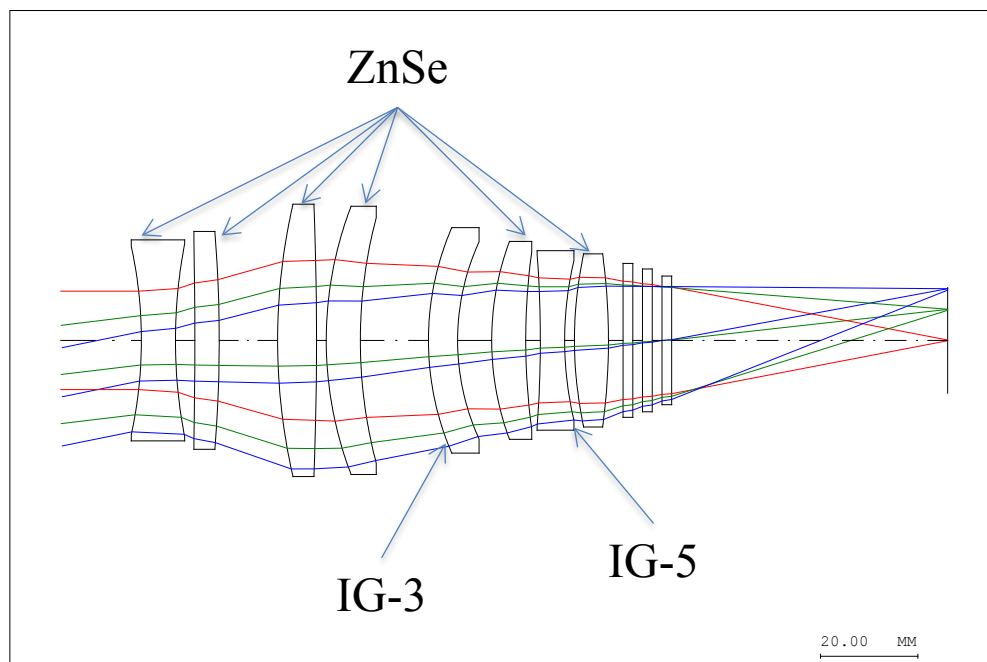


Figure 1: Lens Design Starting Point 53.6mm EFL F/2.68

*Cold Stop and Dewar*

Another appealing feature of the existing lens design is the location of the system aperture stop. The system aperture stop is located external to the lens, in front of the image plane, rather than internal to the lens like a Double Gauss would exhibit. Placing the system stop behind the lens is necessary and critical for infrared applications that utilize cooled detector assemblies in order to couple the lens system stop to the cold shield of the infrared detector assembly. A cold shield is a critical feature installed in the dewar packages of virtually all infrared detectors because they are essential to block unwanted infrared radiation from reaching the sensitive detector elements that make up the focal plane. Cold shields, as their name infers, are cryogenically cooled and limit the field of view as seen by the detector to only include the intended scene, maximizing sensitivity. Therefore, it is important to both couple the exit pupil of the imaging optical assembly to the dewar cold shield, and match the F/# of the optical assembly to the F/# defined by the dewar geometry in order to maintain 100% cold shield efficiency. Systems that are 100% cold shield efficient and properly F/# matched do not waste any signal nor suffer from parasitic signal (Gat et al., 2007). Figure 2, recreated from Gat et al., shows a system with 100% cold shield efficiency on the left, where any extraneous rays outside of the intended field of view do not make it to the focal plane surface. On the right, when coupled to a slower objective lens, the same dewar assembly will operate with less than 100% efficiency, allowing the focal plane to see unwanted parasitic radiation. When the cold shield is 100% efficient, and only then, it is referred to as a cold stop (Fischer, 1992, p. 120). Because the system F/# is defined by the dewar geometry, any attempts at improving performance normally associated with reducing the F/# of the objective lens are unrealized (Riedl, 2001, p. 178).

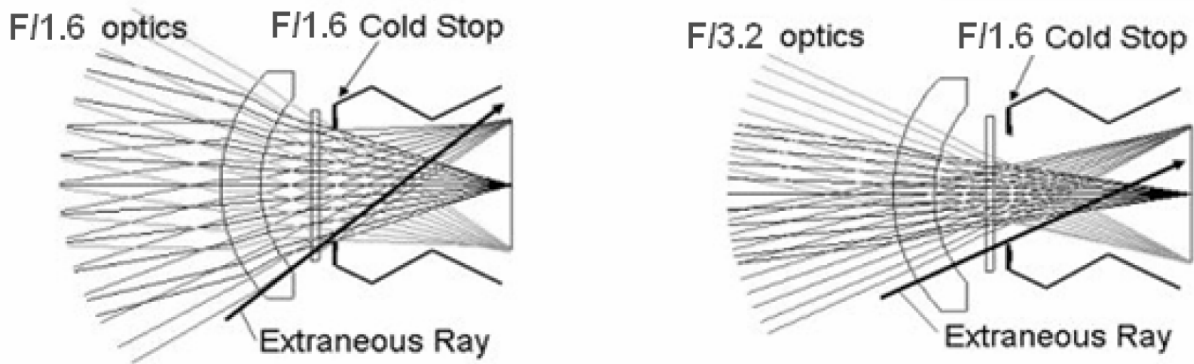


Figure 2: Cold Stop Efficiency and F/# Matching

In addition to a cold stop, a dewar package often includes a protective window and a filter at a minimum, both of which must be accounted for when designing the accompanying lens system. Each window or filter will induce a focus shift to the final image and because this shift is proportional to the index of refraction of the window material, it cannot be overlooked for infrared systems due to the high index of common infrared materials. The customer has defined their dewar configuration, including all windows and filters, which are summarized in Figure 3. The dewar/detector assembly consists of a 16.0mm x 12.8mm image plane, with a 12.7mm diameter cold stop placed 25.5016mm in front of it. Behind the cold stop is a cold filter on a 0.5mm thick Zinc Sulfide substrate, and in front of the cold stop is a 1.0mm thick Sapphire window. Between the lens assembly and the dewar is one of two possible warm filters, each on a 1.0mm thick Zinc Sulfide substrate.

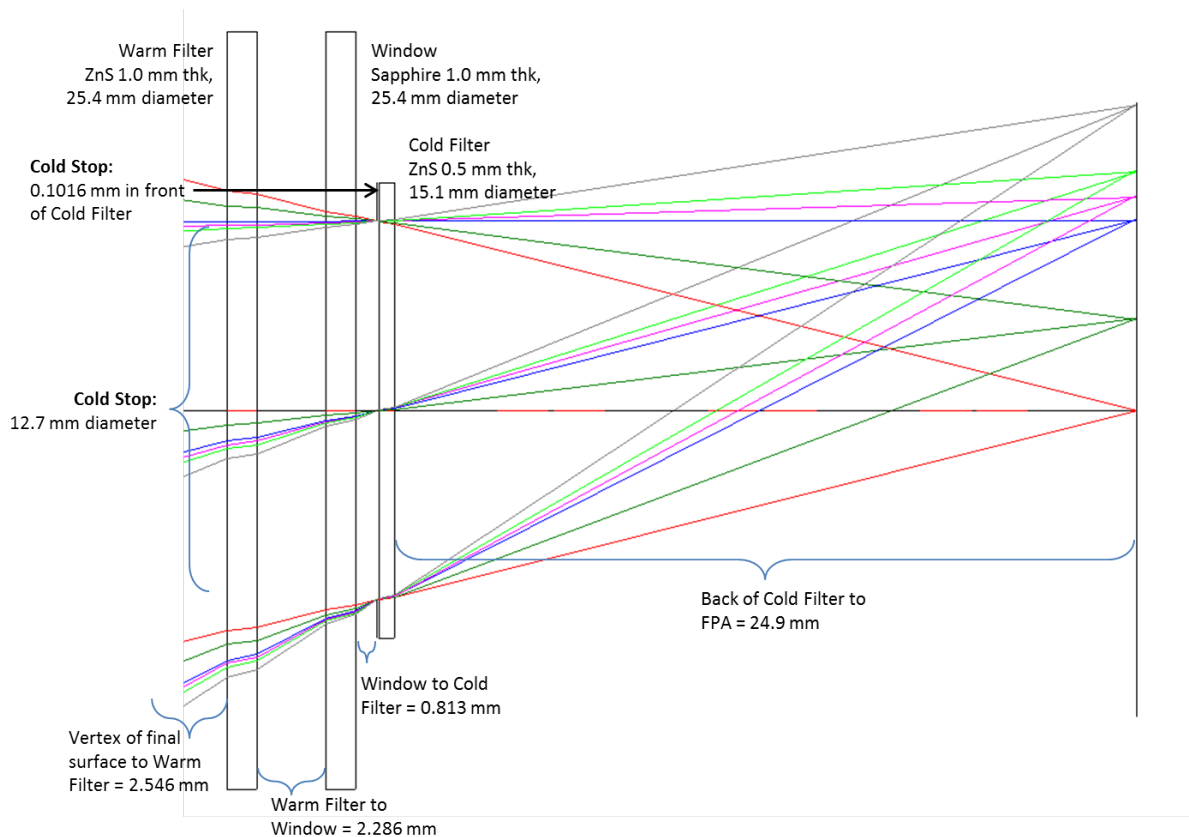


Figure 3: Dewar and Detector Configuration

### *Defining Wavelength*

When designing a broadband optical system, it is important to carefully consider how the wavelength spectrum is defined and weighted. Most of the optical design codes allow the user to specify a limited number of discrete wavelengths rather than a continuous band between two values. Therefore, it is important to sample the waveband with enough points in order to adequately model the behavior of the system. For visible systems, it is standard practice to specify three wavelengths: the F, d, and C Fraunhofer spectral lines, representing wavelengths of 486.1, 587.6, and 656.3 nm, respectively, with either uniform weights of unity, or with weights corresponding to the photopic sensitivity of the human eye. For infrared systems however, the end use application often involves imaging the direct radiation of blackbody sources.

Blackbodies have characteristic spectra defined by their temperature. The spectral radiance from

a blackbody as a function of wavelength is described by Planck's Law of Blackbody Radiation and defined by Equation 1.

$$L_{\lambda} = \frac{2hc^2}{\lambda^5} \frac{1}{\exp(hc/kT\lambda) - 1}$$

Equation 1

To increase the fidelity and accuracy of the optical model, it is necessary to define the wavelengths in accordance with the expected blackbody objects that the system will be imaging. This includes properly weighting each defined wavelength according to the blackbody curve. For this application, the customer has specified a spectrum consistent with a 1000K blackbody source. The blackbody curve associated with this temperature is shown in Figure 4, represented in terms of both normalized radiance and photon output, the former of which includes the relationship between wavelength and energy as defined by the Planck-Einstein relation. As can be seen from the figure, the 1000K blackbody emits the highest radiance at around 2.9 microns, and the highest number of photons at around 3.7 microns. The blackbody emission picks up at 1.0 microns, and extends out well beyond 10 microns. The customer has specified that their detector is sensitive to overall photon count rather than total incident power, and therefore, the red curve of the figure applies. Furthermore, the customer has indicated that their end use application will utilize two separate interchangeable bandpass filters, each appropriate for different viewing environments and conditions. The overall range of the two filters spans from 1.3 to 3.95 microns, which defines the boundaries of the operating spectrum of the lens. Five discrete roughly equally spaced wavelengths between 1.3 and 3.95 microns, weighted according to the red curve of Figure 4, are defined in the optical model of the lens design.

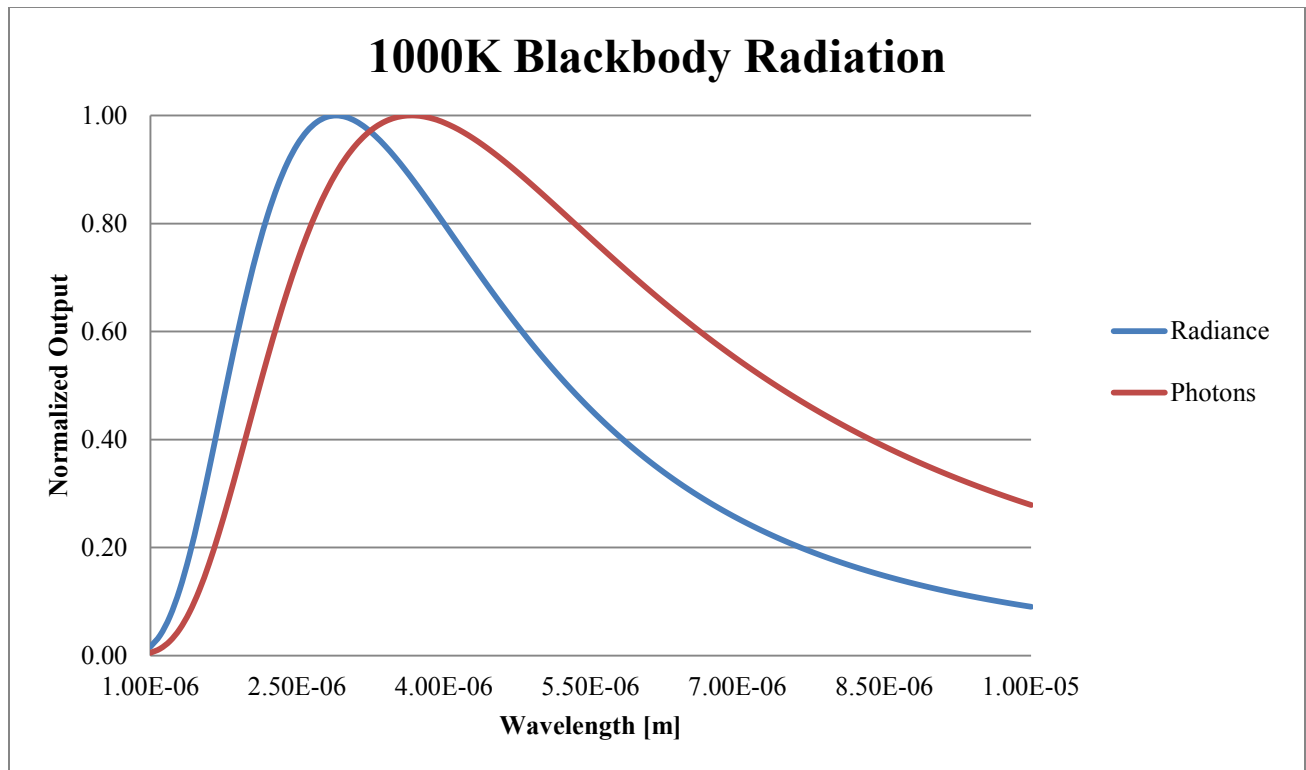


Figure 4: Blackbody Radiation from a 1000K Source

### Scaling and Optimizing

The first step in modifying the existing lens design was to scale it to better match the focal length derived from the Table 1 Requirements. The lens was uniformly scaled from a focal length of 53.6mm to 28.0mm, or in other words, scaled by a factor of 0.52. After applying the scale factor, the image plane dimensions were increased to the values specified in Table 1. Evaluating the encircled energy across this larger field of view indicated that further modification would be necessary to meet the system requirements. This was not surprising, considering that the starting design was likely designed for use with a smaller focal plane. At this point, computer aided optimization would commence.

One of the best features of the Code V software package, the optimization engine, can also become one of its worst, if not properly regulated and supervised by an experienced designer. The optimization routine works by driving the overall error function to a minimum by

changing allowed variables set by the user. Simply setting all lens parameters as variables and hastily defining an error function can quickly result in an optimization that changes the lens design dramatically, and often with undesirable results. Careful consideration must be made to which parameters are allowed to vary, and which are to be frozen. Even more care and thoroughness should be applied when defining the components of the error function, which can include multiple levels of constraints, targets, and inputs, all with applicable weighting as defined by the designer. With every iteration of the optimization routine, the designer should review the resulting solution and make modifications and adjustments as deemed appropriate. By doing this, he will guide the design through design space to the final form.

For the optimization of the SWIR/MWIR objective lens, an error function was defined that specified transverse ray aberration error as the error function type, as this error is closely associated with Ensquared Energy, which is the specified performance requirement metric. A constraint for effective focal length was included to ensure that the resulting solution had a compliant field of view. Variables for the optimization of the scaled starting point design included curvatures of the 16 lens surfaces, and the spacings between lens elements. Additional variables and constraints would be applied as the design developed. The complete evolution of the optical design from the preliminary scaled solution to the final design is outlined in APPENDIX A: EVOLUTION OF THE OPTICAL DESIGN.

### **Final Design and Performance**

The final design, shown in Figure 5, is a 29.77 mm efl F/2 six element compact objective, covering a circular field of view of  $\pm 19$  degrees. Four of the six elements are Zinc Selenide. The second element is made from Calcium Fluoride, and the fifth element is made from IG-3, produced by Vitron for Schott. Two of the 12 element surfaces are aspheres, which were limited

to only Zinc Selenide elements and only to surfaces internal to the lens assembly. Limiting the overall number of aspheric surfaces was done in consideration of cost versus performance, and limiting them to only the Zinc Selenide elements was done in consideration of manufacturing, as Zinc Selenide is a relatively easy material to process with Single Point Diamond Turning, or SPDT. Finally, the aspheric surfaces were limited to interior surfaces only as the marks created by SPDT can be cosmetically undesirable to a customer or end user. By hiding any aspheric surfaces in the interior of the lens assembly, the two externally viewable surfaces are spherical, which can be generated using conventional polishing methods, resulting in smoother surfaces.

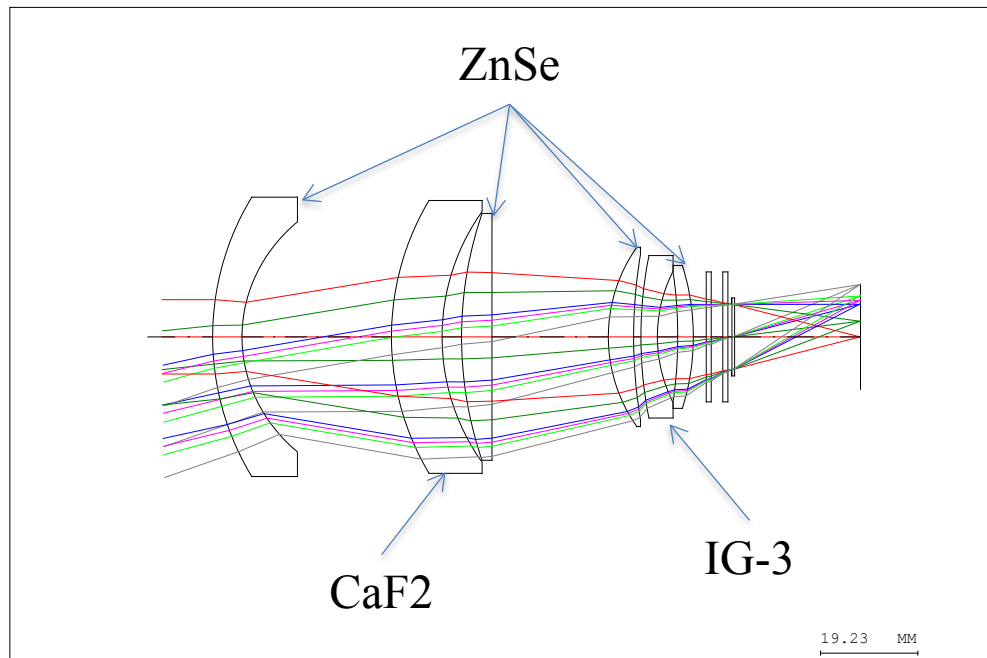


Figure 5: Layout of Final Lens Design

The final optical design is evaluated against all performance requirements using the extensive and various analysis features included in Code V. Code V performs both geometrical and diffraction based calculations to model optical performance characteristics such as Wavefront Error, RMS Spot Size, Encircled Energy, and Modulation Transfer Function (MTF). The following figures represent the as-designed performance of the final design of the objective

lens assembly, not including contributions from manufacturing or assembly tolerances. Table 2 summarizes the compliance of the final design against all requirements and any margin associated with each. Additionally, a full paraxial ray trace and aberration theory calculation is provided in APPENDIX B: PARAXIAL RAY TRACE AND ABERRATION THEORY.

For the purposes of design and analysis, six radially symmetric field points are defined according to Figure 6. Defining too few field points during optimization can result in a lens design that is not consistently corrected over the entire field of view. The six field points are defined as real image heights on the image plane surface. Unlike paraxial image heights, the real image heights include the effects of distortion, and ensure that the correct field of view in object space for a given detector size is calculated as a result.

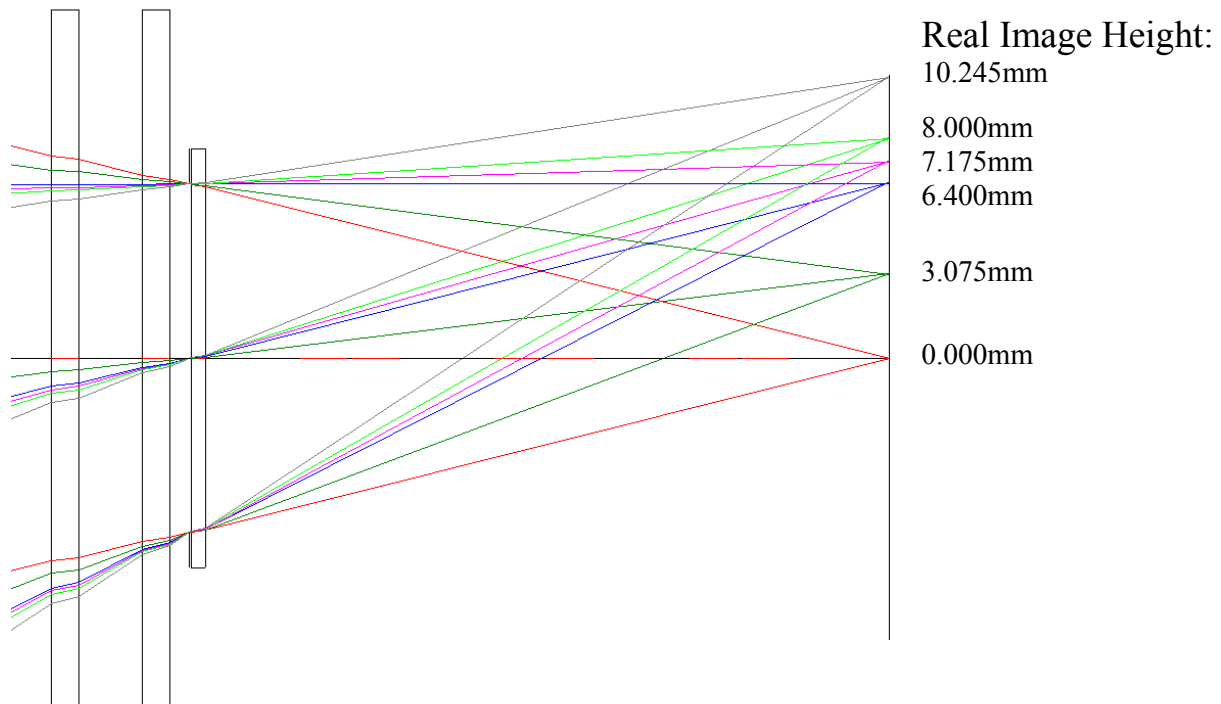


Figure 6: Field Definitions

### *Ensquared Energy*

Encircled Energy represents the ratio of energy of an image point that is focused within a circle of a specified diameter at the image plane. Mathematically, it is determined as the ratio of the 2-dimensional integral of the Point Spread Function over the limits defined by the specified circle, to the same integral over infinite limits. Similarly, Ensquared Energy represents the same ratio, but with the integral limits defined by the specified square. In sensing applications, Ensquared Energy is often specified within a square corresponding to the size of a pixel in the detector assembly. The customer for this application has specified Ensquared Energy over a 25 micron x 25 micron square. In taking a conservative approach, the lens design was optimized and evaluated for Encircled Energy over a 25 micron diameter circle. Because the area covered by a 25 micron diameter circle is completely enclosed by a square with 25 micron sides, as shown in Figure 7, the results obtained from the Encircled Energy analysis are conservative estimates for the resulting Ensquared Energy. Any extra energy not captured within the circle may be picked up within the extra areas at each corner of the square. This practice helps incorporate some extra margin into the design, which helps maintain high yield at the final test phase.

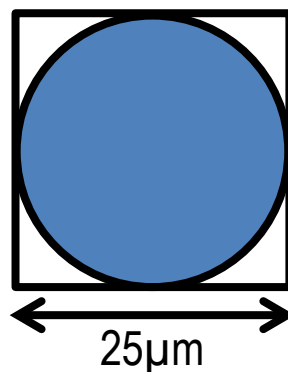


Figure 7: Ensquared versus Encircled Energy

Figure 8 presents the Encircled Energy ratio as a function of circle diameter for the six analysis field points. The results are polychromatic, according to the weighted spectrum defined

by the 1000K blackbody curve. For a 25 micron diameter circle, the on-axis field point achieves 85% encircled energy, and the entire field of view exhibits greater than 77% encircled energy. Diffraction limited performance for this system is represented by the black curve, which shows 88% encircled energy for a 25 micron diameter circle.

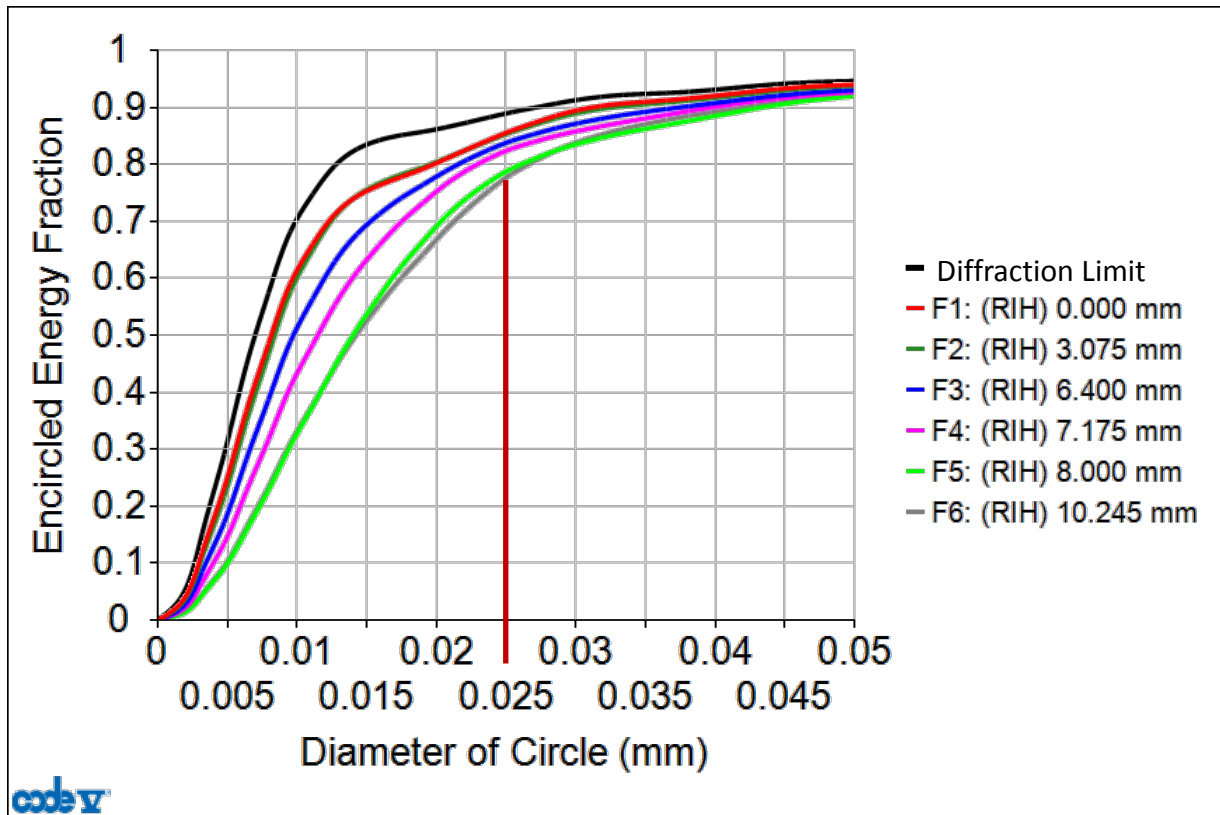


Figure 8: Encircled Energy

Figure 9 presents the encircled energy within a 25 micron diameter circle for six different field heights versus focus position. One can determine many performance characteristics from these through focus curves, such as depth of focus, field curvature, and field tilt. The fact that the peaks of all the curves representing the various field points are well aligned indicates a presence of very little field curvature. The depth of focus for this lens, which represents the longitudinal defocus distance over which the performance requirements are still met, is approximately  $\pm 50$  microns and is limited by the corner field.

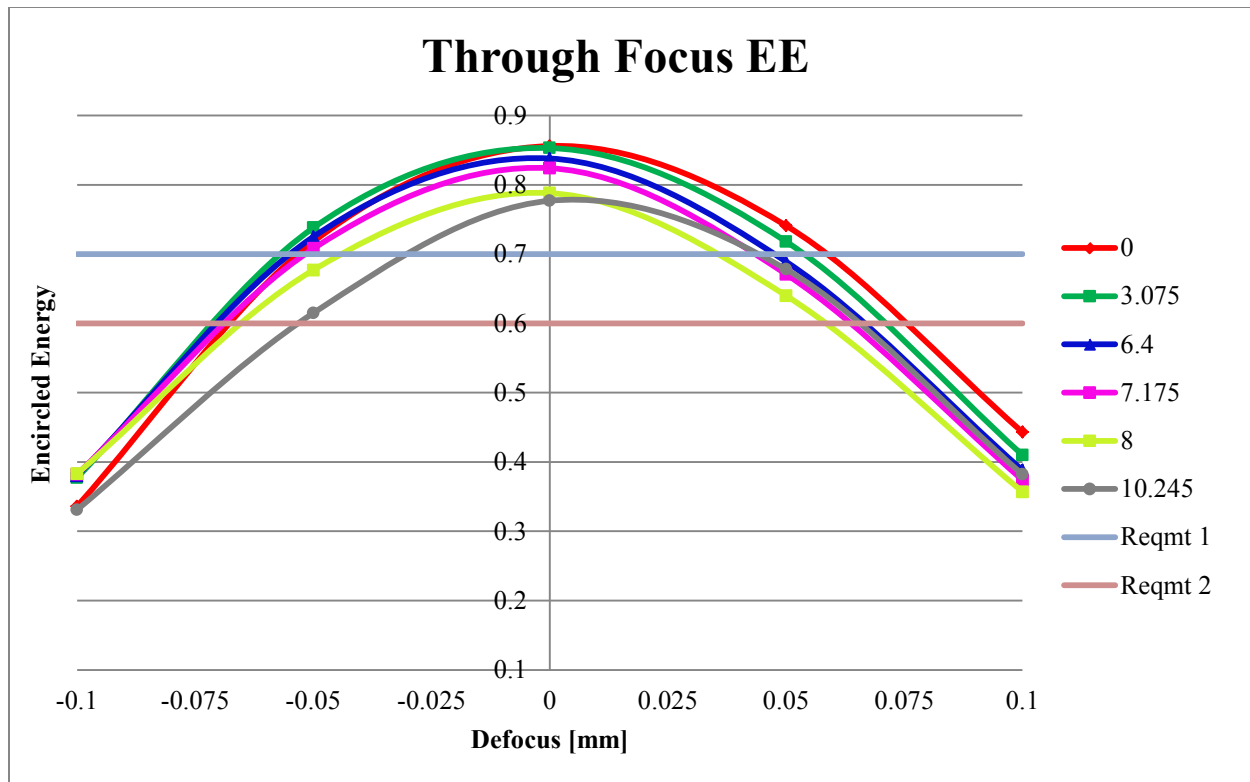


Figure 9: Through Focus Encircled Energy - 25micron diameter

### *Distortion*

Distortion is an aberration that presents itself as a variation in magnification with image height and is the only aberration that does not introduce blur. Low distortion is critical for systems with mapping or tracking applications, as distortion will cause a shift in the mapping between image and object space. For instance, an optical system that is tasked with detecting and tracking the infrared signature of a missile as it is launched and travelling will rely on a strong correlation between the location of the pixel or pixels on the detector array and the corresponding location in object space. For this reason, systems will often be specified to have a maximum distortion of less than a few pixels. A maximum distortion of 2% is allowed for this particular lens, which translates to 205 microns at the corner of the image plane, which is approximately the width of 8 pixels. This lens has an additional requirement that the distortion be correctable to less than 0.1% with only a radial correction term. Often times, if the distortion of

an optical system is well characterized and understood, the effects of this distortion can be corrected or calibrated out of the entire system through software.

There are two types of distortion commonly encountered: barrel and pincushion. Named after the appearances of rectilinear objects imaged through systems with each type of distortion, barrel distortion is negative, and pincushion distortion is positive (Fischer et al., 2008, p. 86). A third, less common type of distortion exists, known as mustache distortion, due to the resemblance of the distortion versus field height curve to a mustache. Unlike barrel or pincushion distortion, where the maximum magnitude of distortion is experienced at the maximum image height from the origin, mustache distortion experiences its extreme value somewhere in between (Hönlinger & Nasse, 2009). This is caused by countermeasures in the design to limit the maximum absolute value of distortion. Figure 10 shows the field curves for this lens design. On the left are the tangential and sagittal focus curves, plotting focus position relative to the image plane versus image height, and on the right is the distortion curve, plotting the relative distortion as a percent of image height, versus image height. As can be seen, this lens exhibits mustache distortion. This was accomplished by adding a constraint to the optimization merit function to deliberately force the distortion to be zero at a non-zero image height. This results in a maximum distortion of less than 0.1% before correction, which equates to 10 microns at the image corner.

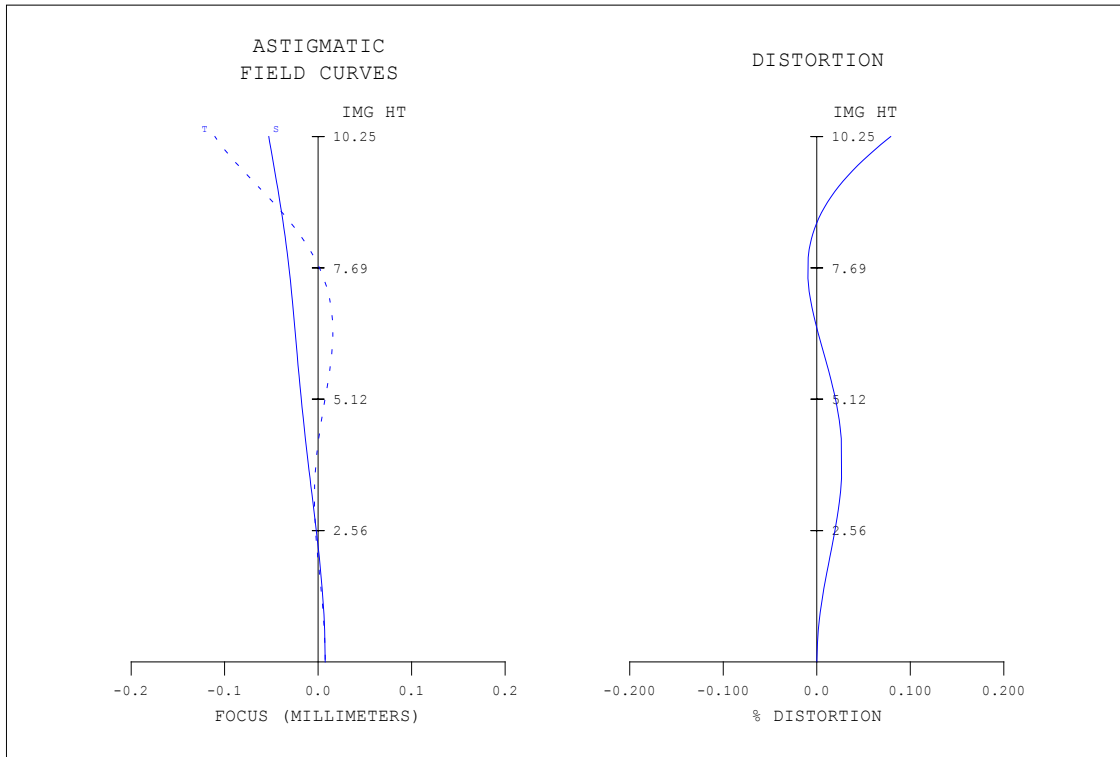


Figure 10: Field Curves and Distortion

### *Relative Illumination*

The relative illumination of this design is presented in Figure 11 and represents the image brightness of a uniformly bright object across the field of view, relative to the on-axis image point. Relative illumination is affected by system transmission, which can vary with field, however in the case of this analysis, transmission was ignored. Table 1 indicates that the requirement for relative illumination is to be greater than 70% at the corners of the image. Figure 11 shows that this design achieves 73.5% relative illumination at the image corner. The drop in relative illumination from on-axis out to the corner of the field is caused by the increasing center ray angle of incidence on the image plane with field height.

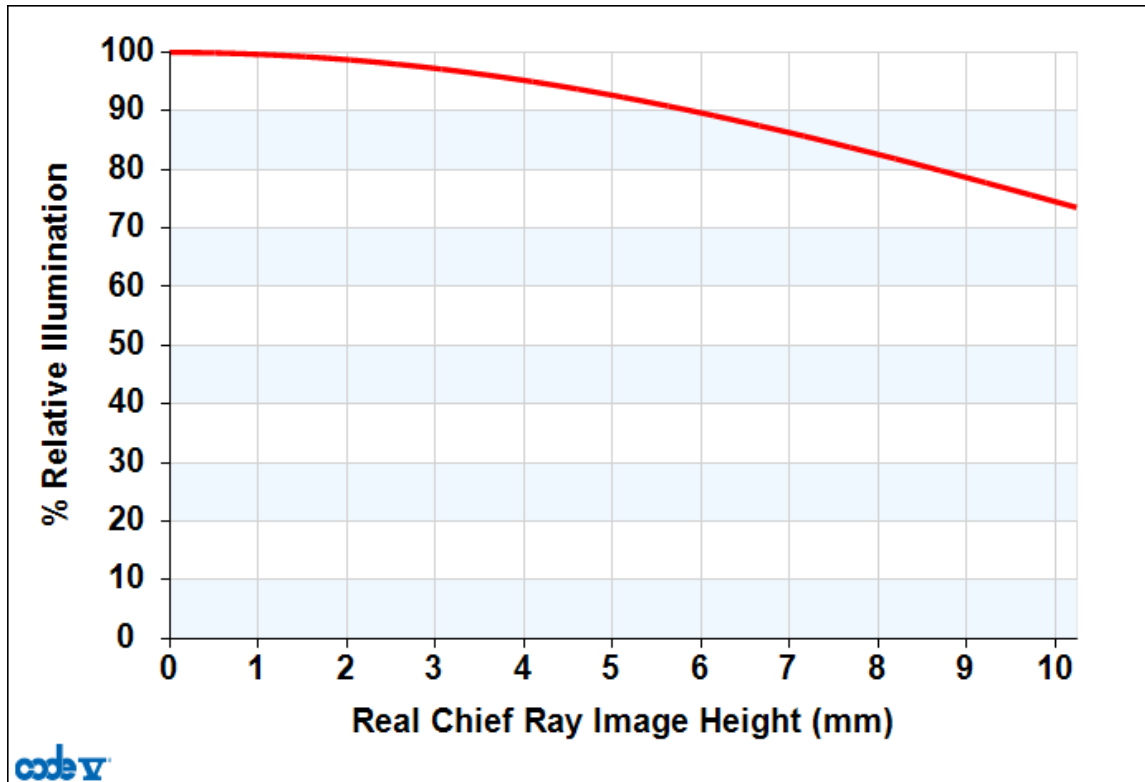


Figure 11: Relative Illumination

### *Modulation Transfer Function*

Although not explicitly specified for this particular lens, the optical performance metrics of MTF and OPD are of enough significance to be discussed here. The Modulation Transfer Function of an optical system defines the modulation, or sometimes contrast, of a black and white line pair of increasing spatial frequency imaged through the system. The modulation transfer function is the autocorrelation of the pupil, and extends to a cutoff frequency determined by wavelength and F/# in the following relationship:

$$v_{cutoff} = \frac{1}{\lambda F/\#}$$

Equation 2

MTF is considered to be the most comprehensive optical system performance criterion for imaging systems, as it directly indicates the image forming quality of a lens for various types of targets (Fischer et al., 2008, p. 191). In most situations, the target or object of interest can be

related to a particular spatial frequency, for which a modulation value can be specified. The classic example of such a target is a white picket fence, which will correspond to a particular spatial frequency at the image plane. The image of this white picket fence will have a modulation value as defined by the system MTF, and that value will relate to the quality of the image. MTF curves are often plotted for both tangential and sagittal (or radial) sets of rays. MTF values are commonly specified for various field points at the Nyquist frequency of the intended detector assembly, which is given by:

$$v_{Nyquist} = \frac{1}{2(\text{pixel pitch})}$$

Equation 3

The Nyquist frequency represents the condition in which one line pair, or cycle, is imaged onto a pair of pixels, one for the light line and one for the dark line of the pair. Frequencies larger than the Nyquist frequency will suffer from a condition known as aliasing. For a pixel pitch of 25 microns, the Nyquist frequency is 20 lp/mm. Figure 12 and Figure 13 show the MTF curves of the objective lens over various spatial frequency ranges. Although this lens was not optimized for MTF performance but rather Encircled Energy, it is not surprising to see that the MTF is near diffraction limited on-axis, and only degrades slightly across the full field of view. Figure 14 shows the MTF values at 20 lp/mm as a function of focus position from the image plane. Similar to the through focus Encircled Energy curves presented in Figure 9, the peaks of the curves representing the various fields are well aligned to one another, once again indicating little to no field curvature.

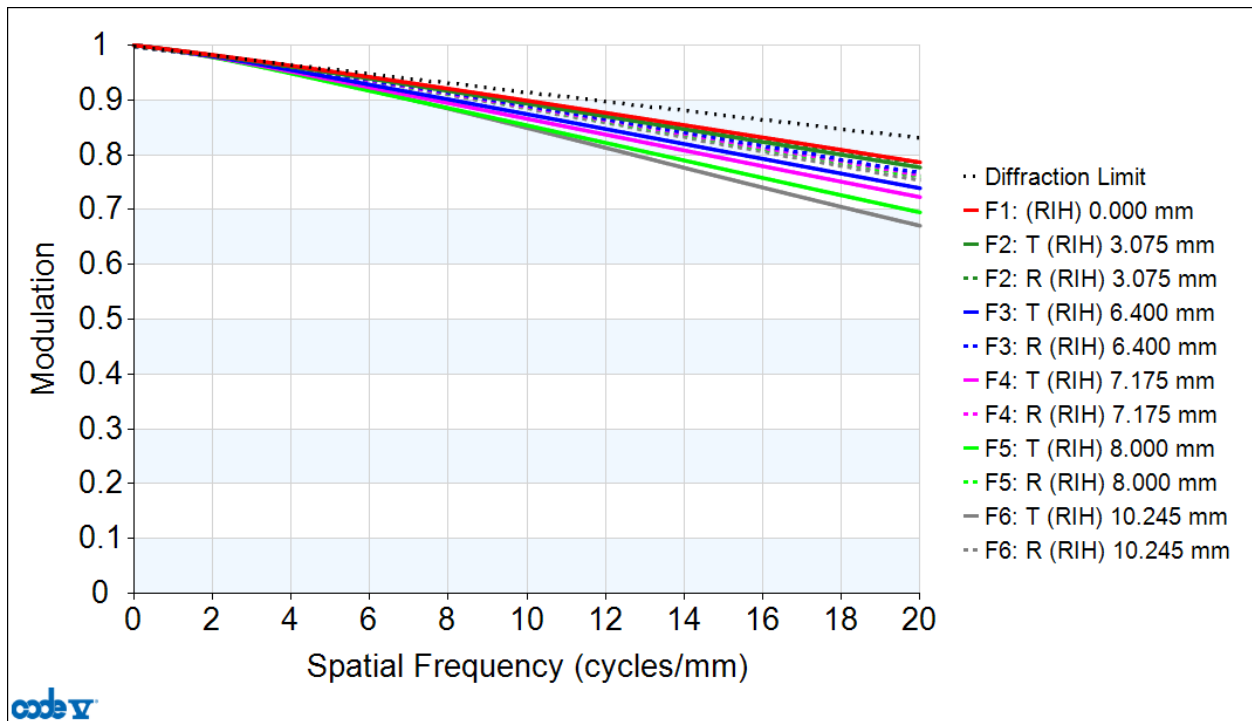


Figure 12: MTF

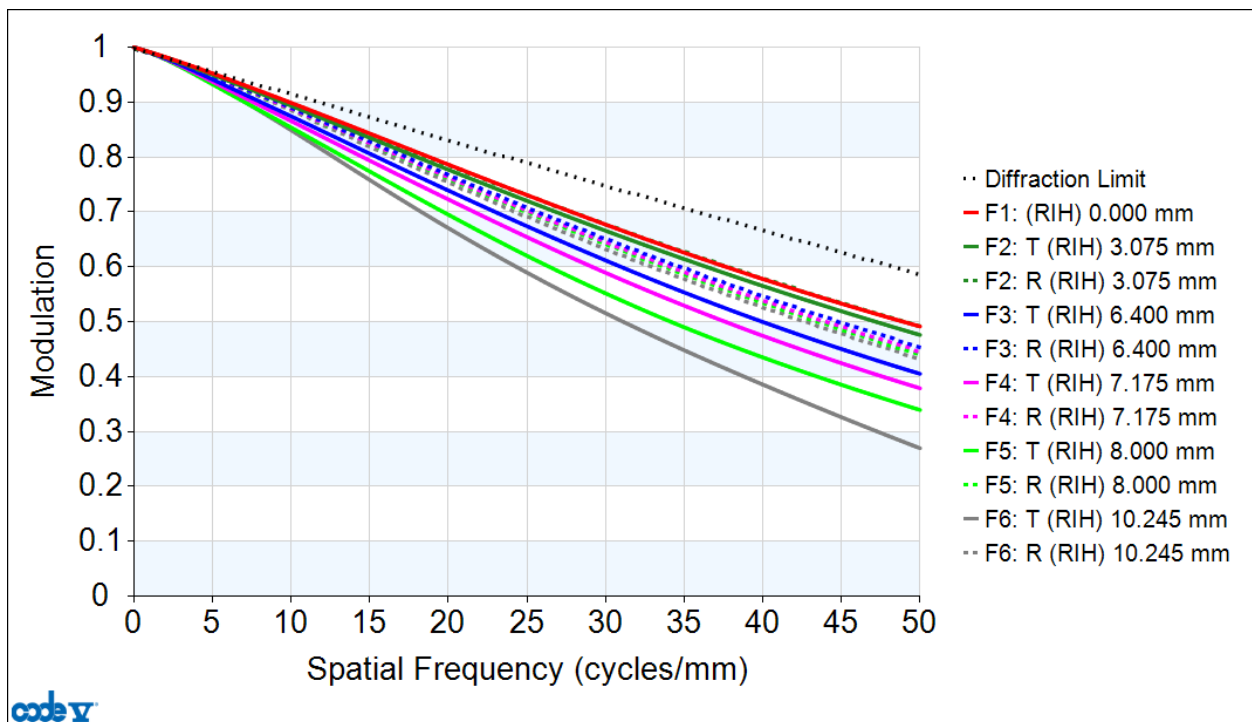


Figure 13: MTF (Increased Spatial Frequency)

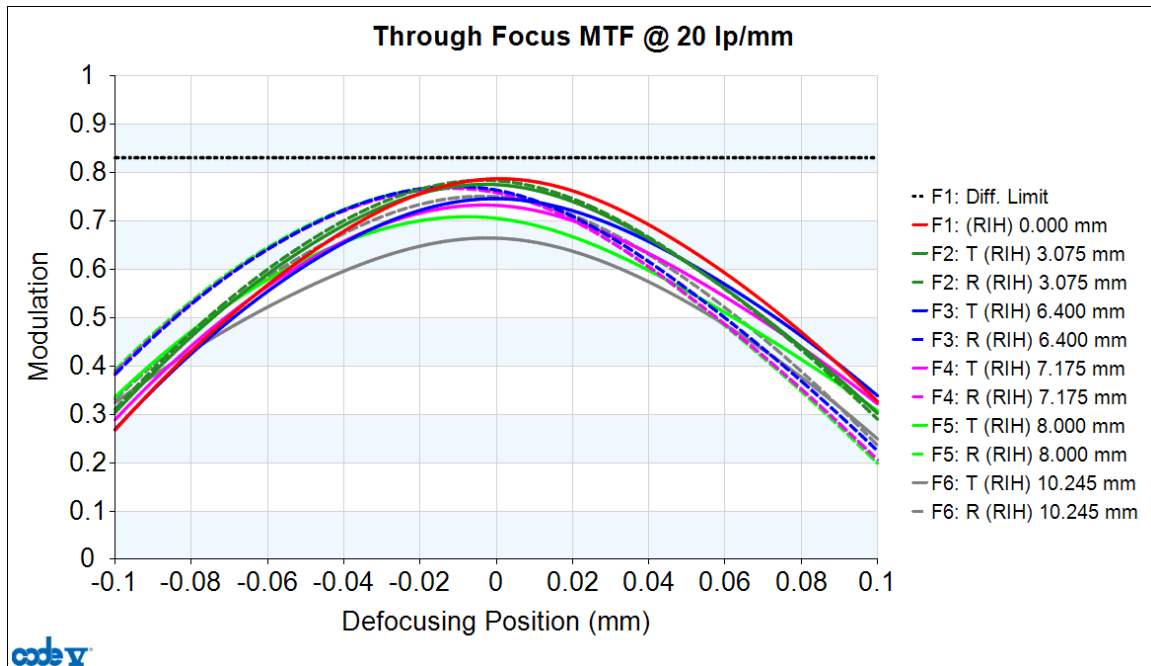


Figure 14: Through Focus MTF

### *Optical Path Difference*

Sometimes referred to as Wave Fans, the OPD fans show the optical path difference between the aberrated wavefront and the perfectly spherical reference wavefront at each specified field height. These plots are a visual representation of the wavefront error as a function of pupil and image height. Multiple curves for each image height can be included on the same plot, corresponding to the multiple system wavelengths. With practice, one can quickly determine the types and magnitude of each of the third order aberrations present, including contributions from chromatic aberrations. The OPD fans presented in Figure 15 show that this lens is well corrected over the full field of view. The fans exhibiting the highest Peak to Valley errors are those that correspond to the wavelengths on the lower end of the spectrum, which happened to be weighted less due according to the 1000K blackbody curve. Therefore, these lesser weighted wavelengths contribute very little to the overall polychromatic wavefront error of the system.

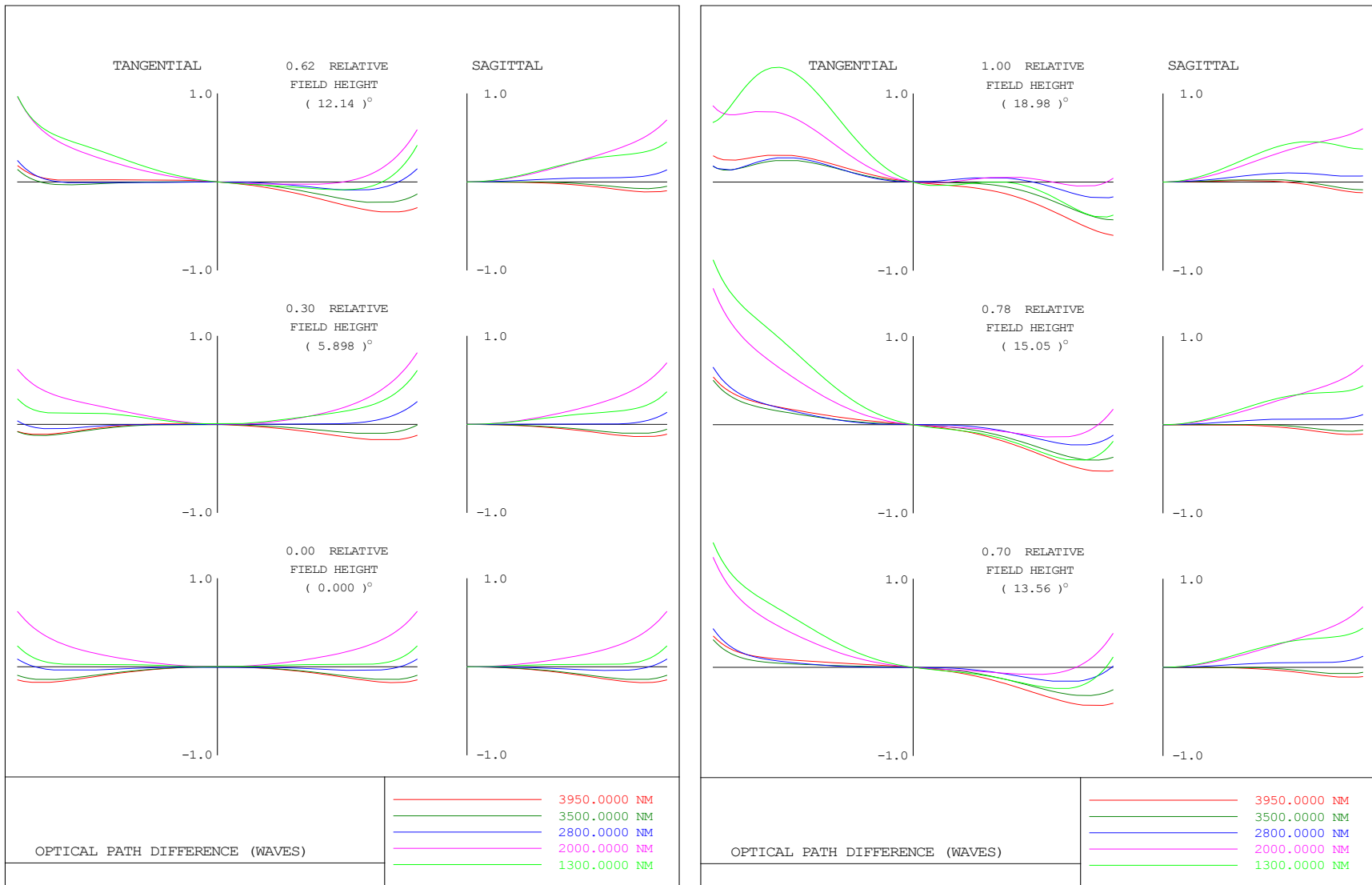


Figure 15: Optical Path Difference

*Design Compliance Matrix*

The nominal design values of various optical performance parameters are compared against their requirements in Table 2. The amount of margin included in the design is calculated and rated according to the Level of Margin key below.

Parameter	Requirement	Design Value	Margin
Field of View	30.00 +0.25/-0.00 degrees Az x 24.20 +0.20/-0.00 degrees El	30.102 degrees Az x 24.279 degrees El	<b>+.102/- .148 Az</b> <b>+.079/- .121 El</b>
Ensquared Energy	>70% within 25 micron square pixel up to ±6.4 mm off-axis >60% within 25 micron square pixel at corners 10.245 mm off-axis	85.6% up to ±6.4 mm off-axis  77.7% at corner	<b>15.6%</b>  <b>17.7%</b>
Distortion	<2% across field correctable to 0.1% with only a radial quadratic correction term	.079% uncorrected	<b>1.921%</b>
Relative Illumination	≥70% at field corners	73.5%	<b>3.5%</b>
Ensquared Energy Depth of Focus	No Requirement	~100 μm	No Requirement
MTF at 20 lp/mm	No Requirement	0.714 AVG of Tan and Sag	No Requirement

Table 2: Design Compliance Matrix

Level of Margin
<b>GOOD</b>
<b>MODERATE</b>
<b>LOW</b>

## Tolerancing

One of the defining practices that signify a lens design that has progressed from the preliminary phase to the final phase is the study and assignment of tolerances. A high performing lens design that suffers significant performance losses under the assignment of achievable tolerances quickly becomes useless. Therefore, the act of tolerancing should be considered an integral step of the design process, and should not be regarded as a mere afterthought. When evaluating the feasibility of a lens design, one must consider the *as-built* performance of the lens, accounting for the effects of the fabrication and assembly processes, rather than just the modeled performance of the bare optical design, which ignores these significant effects.

Generally, once a final optical design has been optimized, the designer will assign tolerances to each parameter and evaluate the sensitivity of the design to each tolerance. Parameters with higher sensitivities will be assigned tighter tolerances, and parameters that are less sensitive will be allowed looser tolerances. The performance degradations due to the effects of each individual tolerance are root sum squared (RSS) together to obtain an estimate of the overall expected performance of the as-built optical system, as described in Warren Smith's paper "Fundamentals of Establishing and Optical Tolerance Budget." Optical designers have practiced this method of tolerancing for decades. However, as the drive for reduced manufacturing costs continues to be a major effort, the approach to tolerancing has evolved.

The method of tolerancing described by Smith is favorable in the sense that it is a good predictor of the overall average performance of a statistically significant set of as-built units. Due to the nature of the RSS approach, the parameters with the largest sensitivities have a significantly larger effect on the overall system performance degradation than the smaller sensitivities. As a result, the approach of reducing, or tightening, the tolerances on the highly

sensitive parameters and loosening the tolerances on the less sensitive parameters was developed. This approach is perfectly rational and effective, so much so in fact, that it is the method behind Code V's Finite Differences algorithm and Interactive Tolerancing feature. Using the Finite Differences algorithm, Code V individually perturbs each of the lens system parameters for which the user has assigned tolerances and calculates the difference in the performance metric for the high and low values of the specified tolerance range. The individual results are then statistically combined to provide an estimate of the total system performance (Hasenauer, 2015). The Interactive Tolerancing feature sorts the results of the individual perturbations in order from highest to lowest. The user can then adjust the tolerances of the most significant and sensitive parameters and see the effects on system performance instantly.

By determining the individual sensitivities of each lens parameter to a set of tolerances, the designer can limit the specification of tighter tolerances to only the parameters that benefit most from them, rather than arbitrarily assigning a blanket set of tight tolerances to the entire system which would most certainly invoke extra and unnecessary production costs.

#### *Code V Reduce Tolerance Sensitivities Feature*

Oftentimes the tolerancing of a lens is performed after the optical design results in a solution that meets the set of performance requirements established at the beginning of the design task. Therefore, the designer may not realize that a design that performs very well "on paper," may be highly sensitive and therefore very expensive and difficult to manufacture until it is too late. To avoid this, Code V has developed and introduced the Reduce Tolerance Sensitivities feature. Also referred to as the SAB (Sensitivity As Built) error function, the Reduce Tolerance Sensitivities option works with Code V's robust and powerful optimization engine to arrive at a lens solution that balances performance with an overall insensitivity to

manufacturing tolerances. The goal of the optimization is to arrive at a design form that meets the as-built specifications with the least expensive tolerance set (Hasenauer, 2015). To utilize the feature, the user will specify the same tolerance value to common parameter types such as center thickness and radius of curvature to a reasonable starting design. The SAB feature will be enabled and added to the error function, variables will be set, and the optimization will run as per usual. However, now the optimization routine will arrive at a solution that is much less sensitive to the effects of tolerances than if the feature were not enabled, which is demonstrated and described in detail by Hasenauer. The overall result is a lens that is cheaper and easier to manufacture, which directly translates to reduced costs. Therefore, it should come as no surprise that the SAB error function was utilized early on in the design process of this high performance F/2 objective lens, and was extremely influential in the final design that has been presented herein.

#### *Final Tolerance Set*

The final specified fabrication and assembly tolerance set is presented in Tables 3-6, and represents mostly standard grade tolerances for a typical optical manufacturing shop. Using the Reduce Tolerance Sensitivities feature resulted in a consistent set of tolerances for all elements, and avoided the need to specify any extremely tight tolerances to any particular parameters. The estimated performance as a result of these tolerances is shown in Figure 16, determined from a simulated Monte Carlo run of 5000 trials.

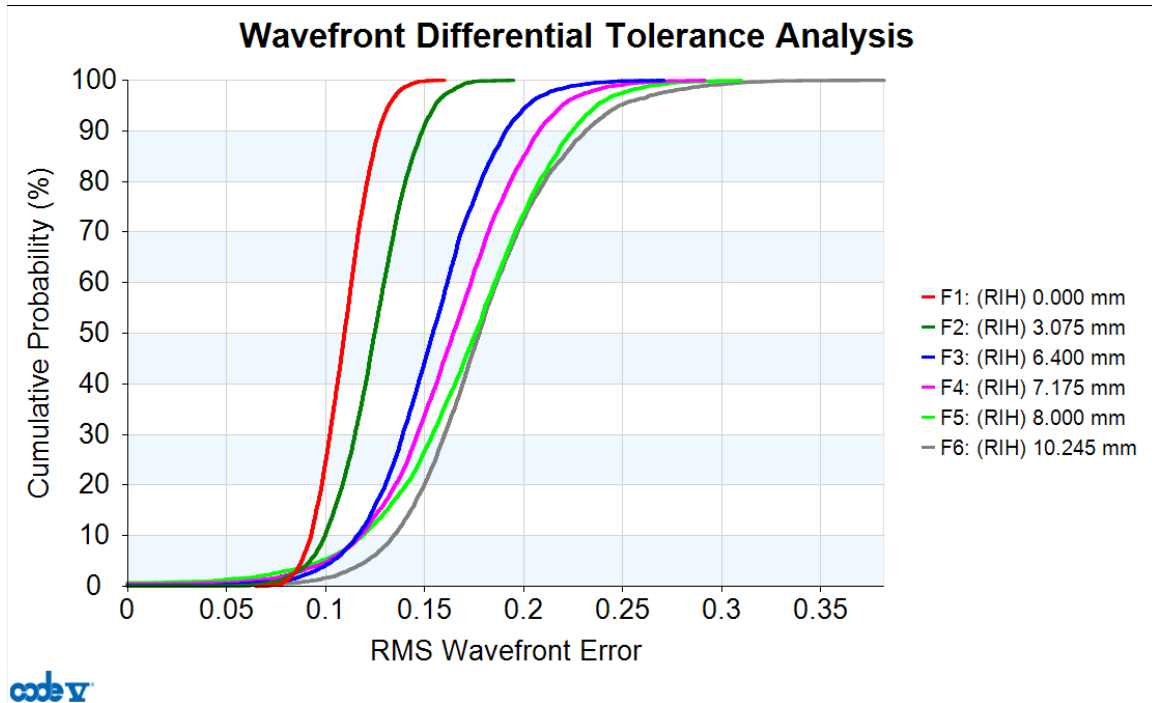


Figure 16: Tolerance Analysis Results - RMS Wavefront Error

With a 97.7% cumulative probability, the estimated RMS wavefront error for each of the six field points is presented below, compared to the nominal design wavefront error for each.

The distance between the lens assembly and the dewar assembly is used as a focus compensator.

RELATIVE FIELD	WEIGHT	DESIGN	DESIGN + TOL *	COMPENSATOR RANGE (+/-) *
0.00, 0.00	1	0.0948	0.1347	DLT S13 0.179287
0.00, 0.30	1	0.1080	0.1597	0.179287
0.00, 0.62	1	0.1285	0.2083	0.179287
0.00, 0.70	1	0.1360	0.2274	0.179287
0.00, 0.78	1	0.1453	0.2462	0.179287
0.00, 1.00	1	0.1362	0.2552	0.179287

Element	S1 Radius [in]	S1 Radius Tolerance		% of Radius	Preferred Mfg Method	S1 IRR Tol [fr]	S2 Radius [in]	S2 Radius Tolerance		% of Radius	Preferred Mfg Method	S2 IRR Tol [fr]
		[in*1000]	[fr]					[in*1000]	[fr]			
1	2.05106	±0.2638	±2	±0.01%	P	±1	1.09185*	±0.1063	±2	±0.01%	D	±1
2	2.03232	±0.2323	±2	±0.01%	P	±1	1.65089	±0.1575	±2	±0.01%	P	±1
3	2.91226	±0.4843	±2	±0.02%	P	±1	INF	-	±2	-	P	±1
4	1.18475	±0.1654	±2	±0.01%	P	±1	3.81417	±1.8661	±2	±0.05%	P	±1
5	3.17624	±1.6339	±2	±0.05%	P	±1	1.10899	±0.2717	±2	±0.02%	P	±1
6	-4.14467*	±3.9567	±2	±0.10%	D	±1	-1.81863	±0.7795	±2	±0.04%	P	±1

Table 3: Element Surface Radius and Irregularity Tolerances

\*Asphere  
fr at  $\lambda=632.8\text{nm}$

P: Polished  
D: Diamond Turned

Element	Diameter [in]	CT [in]	Aspect Ratio D:CT	Material	CT Tolerance [in]
1	2.150	0.22835	9:1	ZnSe	±0.001
2	2.100	0.39370	5:1	CaF2	±0.002
3	2.100	0.23622	9:1	ZnSe	±0.001
4	1.380	0.19685	7:1	ZnSe	±0.001
5	1.250	0.12795	10:1	IG3	±0.001
6	1.100	0.12205	9:1	ZnSe	±0.001

Table 4: Element Center Thickness Tolerances

<b>Airspace</b>	<b>Airspace Tolerance [in]</b>
1-2	$\pm 0.001$
2-3	$\pm 0.001$
3-4	$\pm 0.001$
4-5	$\pm 0.001$
5-6	$\pm 0.001$

Table 5: Assembly Airspace Tolerances

<b>Element</b>	<b>Element Wedge TIR [in]</b>	<b>Element Decenter [in]</b>	<b>Element Tilt [milliradians]</b>
1	0.0010	$\pm 0.0010$	$\pm 0.5$
2	0.0010	$\pm 0.0010$	$\pm 0.5$
3	0.0002	$\pm 0.0006$	$\pm 0.5$
4	0.0010	$\pm 0.0010$	$\pm 0.5$
5	0.0002	$\pm 0.0010$	$\pm 0.5$
6	0.0002	$\pm 0.0010$	$\pm 0.5$

Table 6: Assembly Tilt and Decenter Tolerances

## PART II: OPTICAL COMPONENT FABRICATION AND VERIFICATION

Once the optical design has been fully analyzed, evaluated, and deemed final, the design task transitions to the next phase: preparation for manufacturing. This phase includes the translation of all lens parameters and tolerances into technical drawings, which should include considerations of available manufacturing and assembly processes.

When an optical prescription is developed into an opto-mechanical assembly, considerations must be made for the mounting and assembly of the individual lens elements into the mechanical housing. For instance, adequate margin must be added to each lens surface to allow for mounting and bonding, and clear apertures must be specified for coating purposes. Certain special features are added to each lens to improve the producibility of the assembly.

### **Mechanical Components**

Figure 17 shows a 2 dimensional section view of the complete opto-mechanical assembly. The mechanical design consists of five main components. The optical lens elements are installed into one of two aluminum inner lens cells that are screwed together. Once screwed together, the two lens cells are attached to the stainless steel outer housing, connected by a hollow cylinder of delrin. This delrin sleeve acts as a thermal compensator for the system by expanding at a rate much faster than the aluminum components, which positions the inner lens cell relative to the focal plane to maintain focus over the required environmental temperature range. A stainless steel locking nut is included to lock the position of the objective lens assembly in place at the interface between the objective and the detector assembly once best focus has been set.

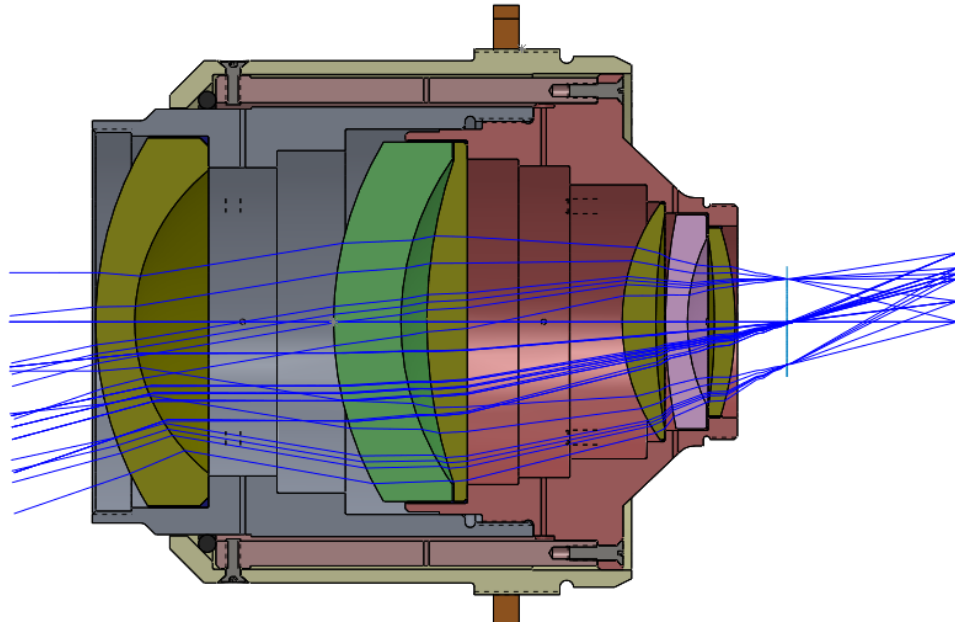


Figure 17: 2-D Section View of Opto-Mechanical Assembly (Dewar Filter and Window elements not shown)

To simplify the mechanical design of the inner lens cell, special features were added to elements 3 and 5 to allow elements 2 and 6 to be bonded directly to them, respectively. A flat flange was added to element 3 and the outer diameter was specified to match the outer diameter of element 2 to allow it to be directly bonded to the seat of element 2. In similar fashion, the seat of element 5 was enlarged to allow element 6 to be bonded directly to it. This effectively reduces the amount of precision mechanical seats required in the inner lens cell. Furthermore, to allow the enclosed volumes of space created by bonding these two sets of elements together, grooves were cut into the seats of elements 2 and 5 to serve as vents to the rest of the lens assembly, to avoid pressure differentials between the various airspaces. Figure 18 is a photograph of surface 2 of element 2 and clearly shows the 4 grooves cut into the seat. Similarly, Figure 19 shows the grooves cut into the seat of element 5.

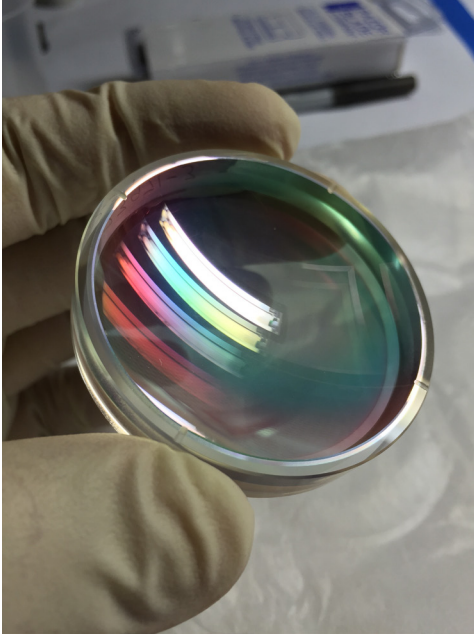


Figure 18: Element 2 – CaF2

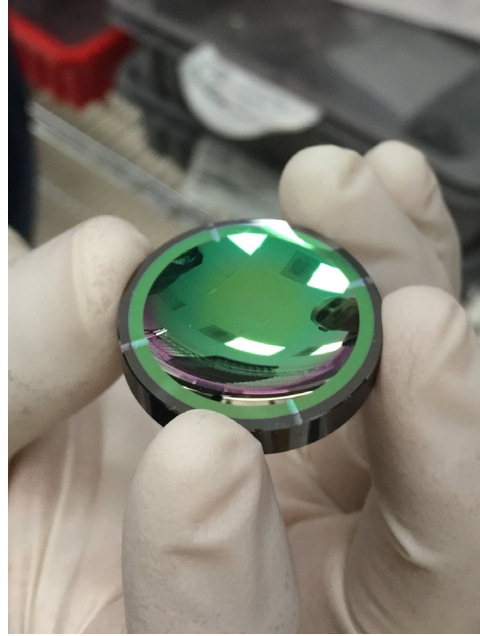


Figure 19: Element 5 – IG-3

In addition to the physical dimensions and geometry of each lens element, the materials from which the elements are to be made from must be accurately specified as well. Optical grade varieties of ZnSe, CaF<sub>2</sub>, and IG-3 were specified and ordered in the form of pucks from reputable vendors around the country. Pucks are oversized cylinders from which lens elements can be fabricated, and are one of the multiple available forms in which material can be purchased. Once received in house, the pucks, also referred to as lens blanks, are processed into lens elements using either conventional polishing or single point diamond turning methods.

### **Optical Component Fabrication Methods**

#### *Conventional Fabrication*

All of the optical elements were fabricated, measured, verified, and coated at II-VI Optical Systems in Murrieta, CA. Elements were fabricated to meet the full set of requirements specified on the drawings. Specific fabrication methods are not called out on the drawings and are left to the discretion of the manufacturer. The CaF<sub>2</sub> element was the only component

completely manufactured using conventional grinding and polishing methods. These methods are referred to as conventional because they have remained essentially unchanged over the past 100 years (Fischer et al., 2008, p. 485). The first step of this process involves grinding the cylindrical puck of lens material and removing material until a spherical shape is formed on one side of the puck. The lens blank is flipped and the opposite side is ground into the appropriate shape. This process is known as generating, as the final product is the generation of a lens blank resembling the shape of the final lens. The next step involves blocking a group of lens blanks to a tool that has a radius similar to the design radius of the lens surface. The block is then subjected to abrasive lapping in sequence with grit of reducing grain size. An optician monitors and controls this grinding process in order to achieve a spherical surface that is very close to the design radius while at the same time minimizing any subsurface damage. The last step of the process involves polishing the surface against a lap with a slurry that has been specially formulated for the particular material (Fischer et al., 2008, p. 486-488). It takes very skilled opticians with significant experience to produce these surfaces to the specified spherical radius of curvature within the power, irregularity, and surface finish requirements listed on the drawing. Once polished, the lens elements are centered and edged to the final outer diameter on a precision lathe.

#### *Single Point Diamond Turning*

Besides the spherical-spherical CaF<sub>2</sub> element 2, the only other surface fabricated using these conventional polishing methods was surface 2 of element 3, which is a plano surface. All other surfaces and elements were fabricated using the methods of single point diamond turning. Diamond turning has become the preferred method for producing aspheric surfaces on IR materials due to its precision and relative practicality compared to deterministic polishing and

magneto-rheological finishing (MRF). Diamond turning a lens surface involves rotating the lens blank about an axis through the center of the lens on a precision chuck, and introducing a fine diamond tipped cutter to the surface as it spins at a high rate of rotation. As the computer controlled diamond tool moves across the spinning surface, the aspheric surface profile is cut into the lens with high accuracy. The resulting surfaces are specular, due to the extremely fine edge of the diamond tipped cutter. This method is just as valid for a spherical surface and other rotationally symmetric surfaces. Another advantage of diamond turning is that the mounting seats and flanges of an element can be produced in the same cut as the optical surface, resulting in highly accurate and flat seats that are perpendicular to the optical axis of the surface, which are crucial when assembling and aligning the elements into the mechanical components. ZnSe happens to be a very suitable material for diamond turning, unlike silicon, which is hard, causing diamond tools to wear out quickly. For these reasons, all 4 ZnSe elements and the IG-3 element were diamond turned, with the exception of the plano surface of element 3. One important feature of diamond turning to be aware of is the generation of shallow concentric grooves in the surface as a result of the cutting process. These grooves are generally of mid-spatial frequency and contribute to surface errors known by the same name. Mid-spatial frequency errors are often over-looked and can seriously degrade the quality of image forming optical systems.

### **Component Verification**

#### *Mid-Spatial Frequency Error*

As described by David Aikens et al. (2008) in the paper, "Specification and Control of Mid-Spatial Frequency Wavefront Errors in Optical Systems," mid-spatial frequency errors are caused by modern deterministic optical fabrication techniques and are represented as residual small amplitude periodic surface undulations. Commonly referred to as waviness or ripple, mid-

spatial frequency errors fall in the frequency regime between long scale form errors, and short scale roughness errors. Mid-spatial frequency errors erode the peaks and nodes of the point spread function, causing a deleterious effect on image quality (Aikens et al., 2008, p. 2). For high performance systems that have been determined to be sensitive to mid-spatial frequency ripple error, the error should be tolerance and specified just like any other fabrication or assembly tolerance.

Using the Code V RPA tolerance type, the sensitivity of each surface to various amplitudes and frequencies were analyzed. The results are included with the full set of tolerance sensitivities in APPENDIX C: TOLERANCE SENSITIVITIES. Following the example presented by Aikens et al. (2008), mid-spatial frequency errors are controlled and specified over a frequency range defined by a band pass filter. The low frequency cutoff is specified as 5 cycles across the aperture of the surface, and the high frequency cutoff is calculated from the scale length whose Fresnel distance is one tenth that of the imaging distance from the surface to the image plane. Once these frequency regions are determined for each surface, the RMS amplitudes of the allowable error within these regions are chosen according to the results of the sensitivity analysis.

#### *Interferometric Verification of Spherical Surfaces*

All spherical surfaces were measured and verified on a Zygo GPI XP/D 633nm phase-shifting interferometer. Various 4-inch  $\lambda/10$  transmission spheres were used to measure each surface over the full specified clear aperture. Radius of curvatures were verified using a highly accurate radius bench by measuring the distance from the cat's eye position to the confocal position, which is achieved by nulling the interferogram. Surface irregularity was reported as the residual surface error once piston, tilt, and power had been removed. Mid spatial frequency

errors were verified by applying a band pass filter to the measurement according to the drawing specifications. Figure 20 shows an example of a surface figure measurement for surface 1 of an element 1 without filtering applied, resulting in 20.65 nm RMS surface error, and Figure 21 shows the same measurement with filtering applied to include only the mid-spatial frequency errors between 0.11111 and 2.56410 cycles/mm, resulting in an error of 5.55 nm RMS.

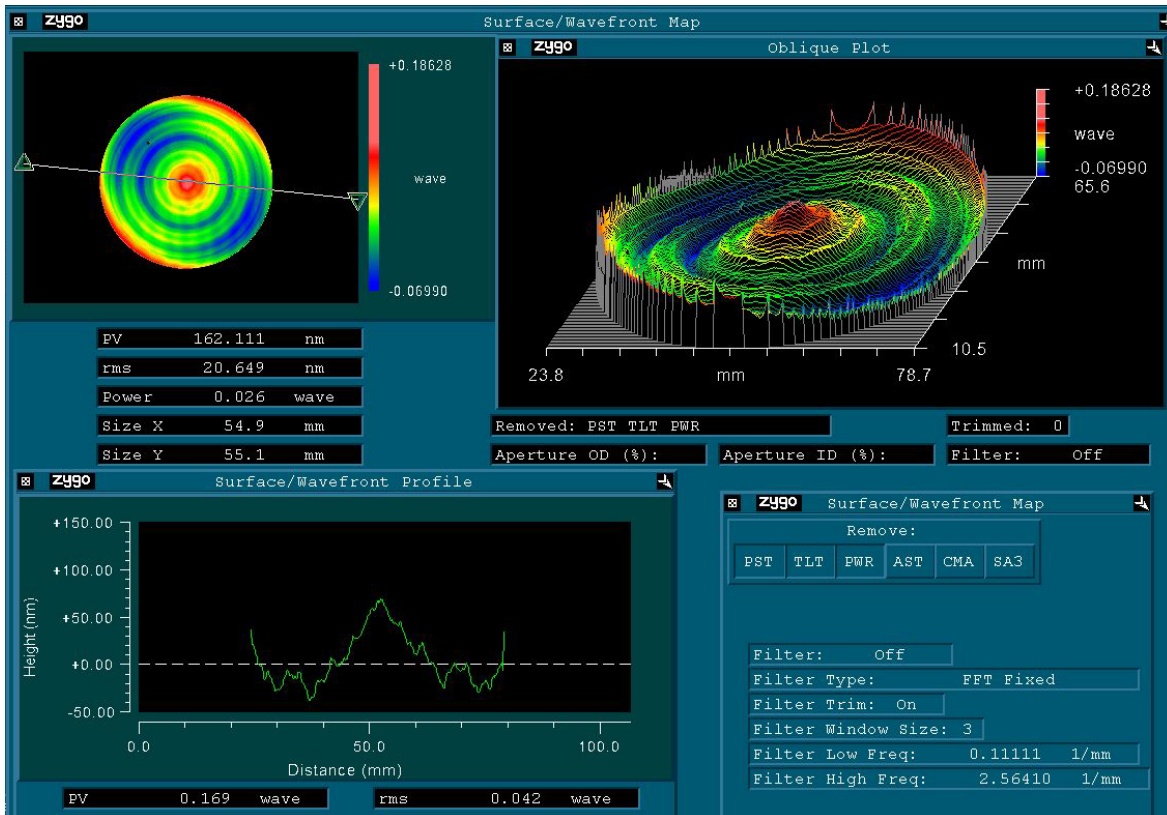


Figure 20: Element 1 Surface 1 Surface Figure Measurement without Mid-Spatial Frequency Filtering

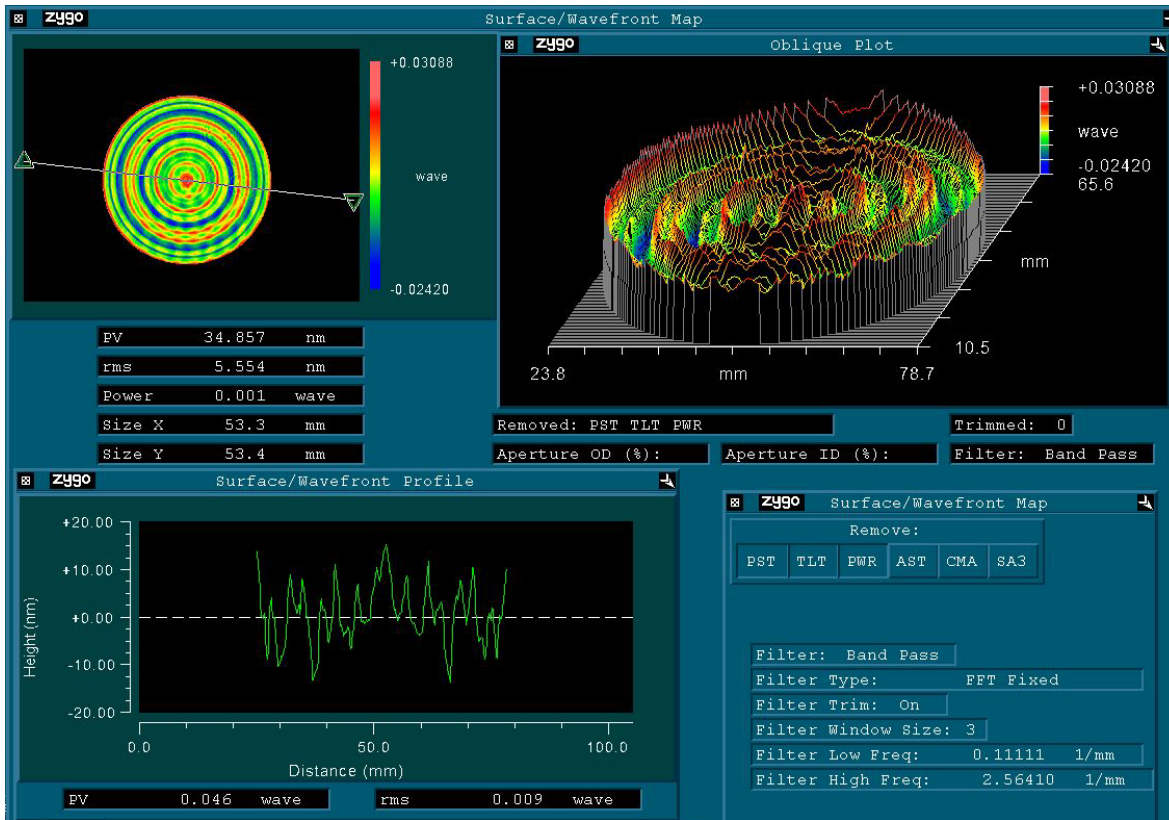


Figure 21: Element 1 Surface 1 Surface Figure Measurement with Mid-Spatial Frequency Filtering  
*Profilometer Verification of Aspheric Surfaces*

The two aspheric surfaces were verified using a Taylor Hobson Form TalySurf profilometer by tracing a probe over the surface in orthogonal orientations. Although not providing a full aperture surface measurement like an interferometer, the Form TalySurf profilometer has been an industry standard tool for verifying aspheric surfaces since its introduction in 1984 (Taylor-Hobson, 2015). Other full aperture methods include the utilization of null optics or CGH nulls with a classical spherical interferometer, or direct measurement with special stitching interferometers such as the ASI by QED Technologies, which uses a specialized variable optical null device consisting of two counter-rotating optical wedges. By varying the rotation and tilt of the two wedges, varying amounts of compensating error can be produced in order to obtain measurements over multiple sub-apertures. These highly capable advanced

stitching interferometers can measure full aperture aspheric surfaces with up to a thousand waves of departure from a sphere. Nevertheless, the resulting height profiles measured from the profilometer traces were individually fit to best fit radii, which were compared and reported as the surface base radius of curvature. Then, the design aspheric coefficients were removed from the profile and the resulting error was reported as the surface irregularity. Finally, the remaining irregularity was filtered according to the drawing specifications and the residual error was reported as the mid-spatial frequency error of the surface. Figure 22 shows an example of a TalySurf trace for the aspheric surfaces from surface 2 of one of the element 1's.

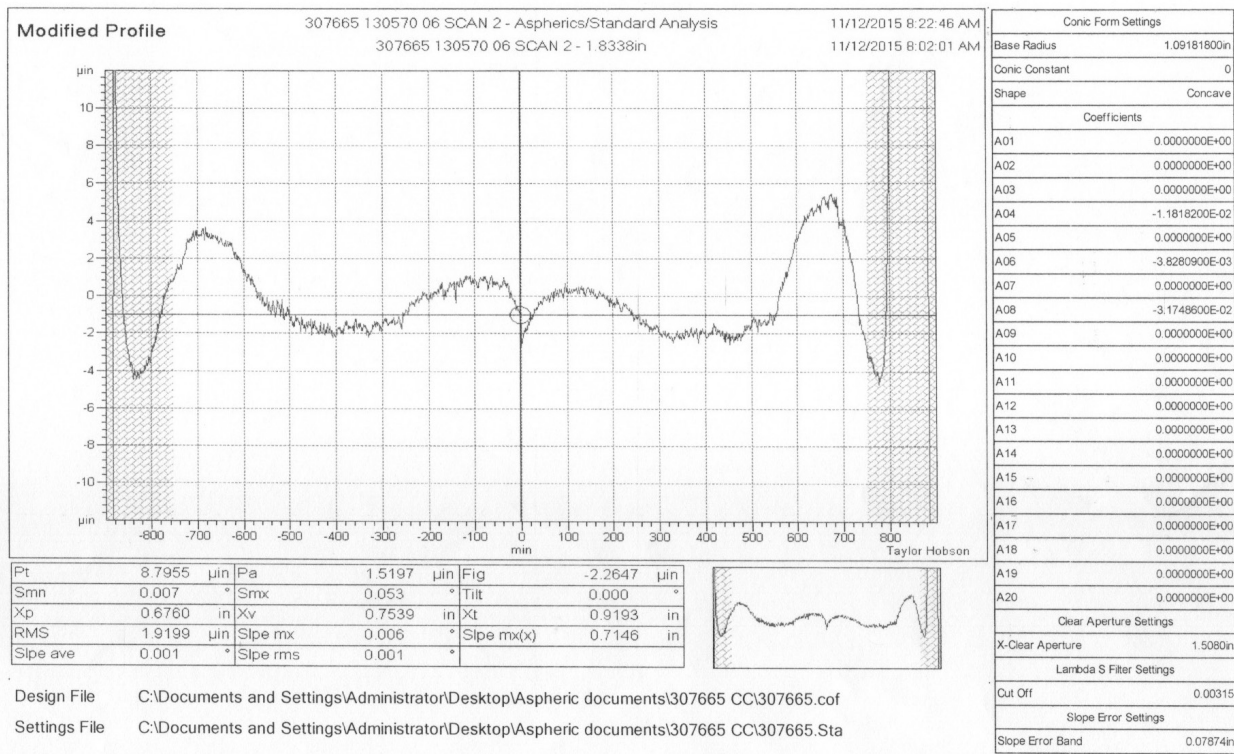


Figure 22: Single TalySurf Scan of an Aspheric Surface

### *Surface Roughness Verification*

Finally, all surfaces are measured for surface roughness on an ADE Phase Shift MicroXam non-contact optical profilometer. Surface roughness, which is a surface error in the high spatial frequency region, is measured over multiple 809 micron x 612 micron areas on each

surface. Surface roughness, also classified as surface finish, is primarily a result of the surface generating process and depends on the substrate material. Surface roughness is controlled to prevent losses due to scattering, which is inversely proportional to wavelength squared, and for applications in the MWIR, is commonly specified as less than 60 Angstroms rms. Achieving this level of surface roughness on diamond turned ZnSe and IG-3 surfaces is realized without much difficulty, and even smaller surface roughness values can be achieved with conventional polishing methods.

### **Anti-Reflection Coatings**

After the lens elements have completed fabrication and surface verification, the optical surfaces are coated with multi-layer anti-reflection coatings in order to reduce the Fresnel reflection losses at each air to surface interface. Multi-layer broadband coatings can be designed to have low reflectivity over fairly broad wave bands, and for large ranges of angles of incidence without much effort up to certain limits. At some point, broadening the wave band over which the coating exhibits low reflectivity becomes increasingly difficult, requiring more and more layers. The topic of thin film deposition techniques and technology is beyond the scope of this report, however there are numerous excellent references on the subject by world renowned experts in the field including H. Angus Macleod and Charles M. Falco, both affiliated with the University of Arizona's College of Optical Sciences.

Lens elements of the same material are coated in batches according to the size of available coating chambers. Only elements of the same material can be coated at the same time, as the coating designs are unique for each substrate material. Each lens surface is coated over the entire clear aperture, which is achieved through the use of specialized coating tooling. Once coated, each surface is subjected to a series of environmental tests as specified by MIL-F-48616,

including temperature, humidity, abrasion, and adhesion tests. Testing the coatings to these specifications help ensure that the coatings will remain adhered to the lens elements and survive the various operating environmental conditions.

Elements that pass these environmental tests are cleaned and inspected for final surface quality, which is a measure of any scratches and digs on the surface, commonly specified by MIL-PRF-13830B. These surface quality requirements can be specified as dimensional requirements, or more often, as comparative requirements against a set of scratch/dig standards. Surface imperfections such as scratches and digs can be sources of scattered light, or can result in fracturing and other substantial damage when used in high-energy laser applications. It is the responsibility of the optical designer to understand the end-use application of the lens elements and specify the surface quality requirements appropriately. In the case of these elements for the SWIR/MWIR objective lens assembly, neither scatter from small scratches and digs nor absorption of high levels of energy is a concern, and therefore, the surfaces are specified to a surface quality of 60-40 per MIL-PRF-13830B for cosmetic and workmanship purposes, which is considered standard grade in many optical fabrication shops. Elements that meet the full set of component level requirements are kitted for delivery to final integration and assembly. Elements that are non-compliant to any requirement are re-worked, and if re-work is not possible, they are scrapped.

### PART III: ASSEMBLY

Assembly of an optical system is what transforms the individual components into a high performance opto-mechanical imaging system. The assembly methods and tools must be capable of achieving the specified assembly tolerances and targets, or else the final assembled unit will fail to meet the performance requirements. For this reason, it is important for the designer to understand the capabilities of the available instruments and allocate tolerances appropriately in order to achieve a high production yield. As a result of the Reduce Tolerance Sensitivities feature of the Code V optimization, the resulting assembly tolerances are achievable through common practices without much difficulty. All lens elements are actively centered in their corresponding mechanical seats using feedback from a Trioptics OptiCentric device.

#### **Assembly Methods**

Manufactured by Trioptics, the OptiCentric Alignment Station is equipped with two autocollimators and a precision air bearing assembly, and is capable of measuring centration errors to less than a micron. The basic operation involves adjusting the top and bottom mounted autocollimators to retro-reflect off the front and rear surfaces of a lens element that rests on the air bearing. The individual centrations of the surfaces relative to the rotational axis of the air bearing stage are measured from the displacement of the circle traced by the retro-reflected spot on the detector of each autocollimator. The lens is continuously adjusted in centration and tip/tilt using kinematic mechanical interfaces until the target centration error is achieved.

An optical element is perfectly centered when the centers of curvature of each surface lie on the same axis. Because the lens elements in this lens assembly have seats cut into them for mounting purposes, these seats need to be perpendicular to the axis defined by the centers of curvatures of each surface. The high accuracy achievable with diamond turning results in lens

elements that have little to no wedge and seats that are perpendicular to optical axis of the lens. This aides in the assembly centration process because it means that when the top surface of the lens is positioned to be centered to the top autocollimator, the rear surface is also very well centered to the same axis.

### *Aft Cell*

The first step of the assembly process is to mount the aft mechanical cell to a kinematic mount installed on the air bearing stage. The mechanical seat of lens element 5 is aligned perpendicular to the axis of the autocollimator by reflecting off a very flat and parallel piece of sapphire placed directly on the lens seat. In addition, the seat is centered relative to the air bearing by performing a total indicated runout measurement. Once the seat has been aligned to the autocollimator, the autocollimator serves as the reference for alignment of the lens element. The lens element is carefully placed onto the mechanical seat and the top surface is actively aligned to the top autocollimator. Although the centration targets have been specified as  $\pm 25$  microns per element ( $\pm 15$  for element 3), centration errors of less than  $\pm 10$  microns were consistently achieved using these methods. Once element 5 has been fully aligned, it is bonded into place using an ultraviolet cured tack. The tack bond is a fast-curing method used to hold the lens element in place while the permanent polyurethane adhesive is shot complete around the lens element. Once the polyurethane has completely cured, the tack bonds are removed.

This general procedure is repeated for the remaining lens elements, with minor modifications specific to each element. For instance, the seat of element 2 is placed directly on top of the flange of element 3, and the two elements are centered to each other using the OptiCentric. The two elements are edge bonded together and then installed into the mechanical cell and aligned as if they were a single lens element. Every element is centered to the previously

installed elements using the surfaces that are facing the top autocollimator. The centrations of the opposite surfaces are not monitored due to limitations of the visible source in transmitting through the AR coatings applied to the infrared lens elements. Therefore, the entire centration procedure relies on the fabrication of each element with small amounts of wedge.

Element 6 is the only element whose mounting seat is on surface 1 instead of surface 2, and therefore the mechanical cell is flipped upside down so that element 6 can be seated directly onto the mechanical seat created by the oversized seat of element 5. Figure 23 shows a photograph of the aft lens cell installed upside down into a specialized kinematic tool. The dark gray concave surface visible at the top of the cell is the second surface of lens element 5, onto which element 6 is directly placed.

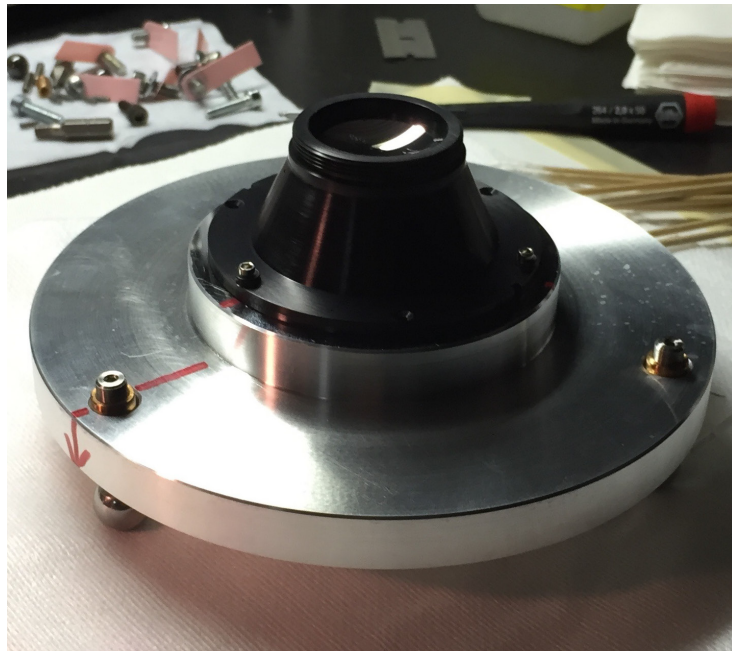


Figure 23: Aft Cell in Kinematic Mount Tooling

### *Forward Cell*

Before element 1 is installed, the forward lens cell is screwed onto the aft lens cell through a precision interface. The surfaces at the interface are tightly toleranced so that the proper spacing to the element 1 seat is maintained. Once screwed together, element 1 is centered and bonded following the same procedure outlined earlier. Figure 24 shows a photograph of element 1 installed into the forward lens cell and held in place with tack bonds. Figure 25 shows a cross section model view of all 6 elements installed into the aft and forward mechanical cells after they have been screwed together, mounted to the kinematic tool (purple).



Figure 24: Element 1 tack bonded into Forward Lens Cell

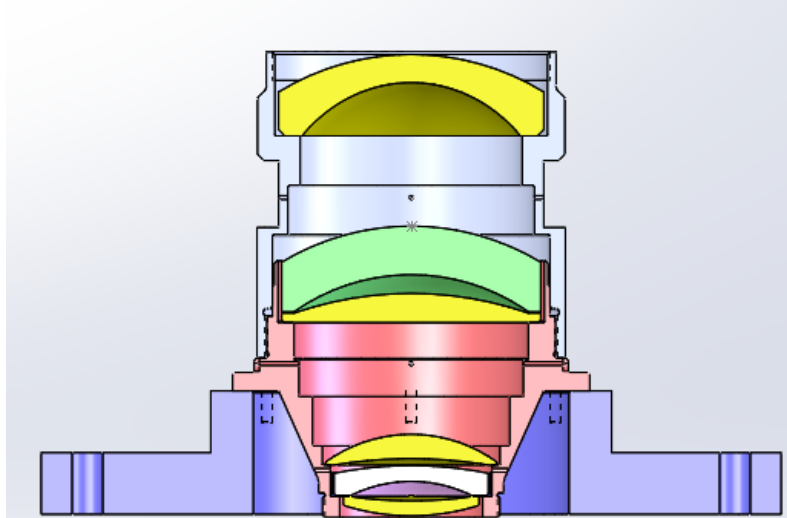


Figure 25: Cross Section of Mechanical Cell Mounted to Kinematic Tool

### *Delrin Sleeve and Outer Housing*

When all 6 elements have been bonded into the two-piece mechanical lens cell, the Delrin sleeve is slid over the lens cell and attached at six points using small screws. Then, the outer stainless steel housing is slid over the Delrin, and attached on the opposite side using six small screws. Finally, the stainless steel locking ring is installed, completing the assembly of the Objective Lens. An exploded view of the main mechanical components is shown in Figure 26. Photographs of fully assembled units are shown in Figure 27 and Figure 28.

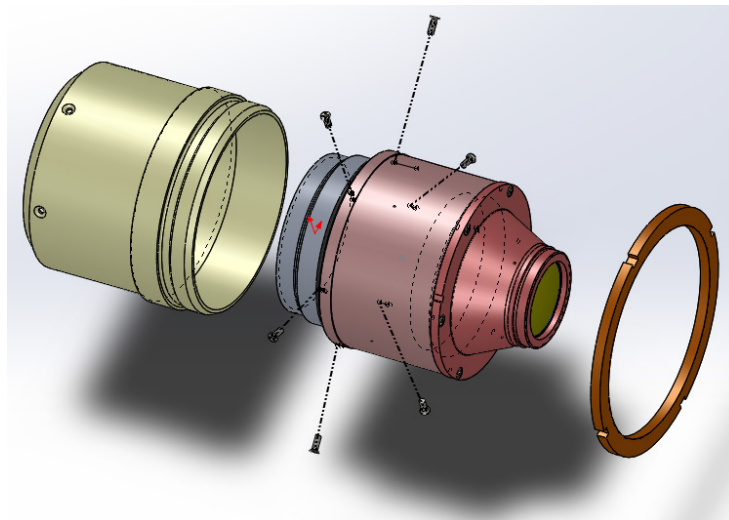


Figure 26: Exploded View of Main Mechanical Components



Figure 27: Objective Lens Assembly - Front

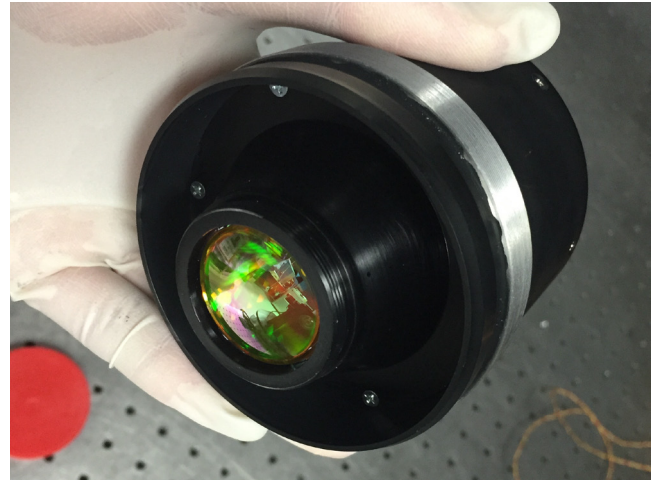


Figure 28: Objective Lens Assembly - Rear

#### PART IV: SYSTEM TEST AND FINAL AS-BUILT RESULTS

Once the units have been assembled, they are submitted for final system level testing. A custom test bench has been developed for the automated testing of completed objective lens assemblies. All 41 objective lens assemblies were subjected to the complete test program as they completed assembly over the course of a few months. With the exception of only a few units, all lens assemblies passed all requirements and showed good correlation to one another. Comparing the test results of the as-built units to the predicted design values also showed a strong correlation, indicating a high fidelity model and an accurate understanding of the fabrication and assembly processes.

#### **Test Setup**

A custom test bench consisting of a chopped blackbody source, an off-axis parabola, and an InSb detector assembly has been designed and built for testing the SWIR/MWIR Objective Lens Assembly for compliance to the set of customer specified requirements. Through the use of computer controlled stages and custom software, the measurement of a lens and the collection of data is entirely autonomous, and takes approximately 4 hours per lens assembly.

Figure 29 shows a basic layout of the specialized test bench setup used for the measurement of these lens assemblies (Holloway & Weed, n.d.). A high emissivity temperature controlled blackbody source is placed behind a small pinhole, which is precisely positioned at the focus of a high quality off-axis parabolic mirror. A small fold mirror is utilized between the blackbody source and the off-axis parabola for space considerations. This setup produces a collimated wavefront of infrared energy directed toward the objective lens assembly under test. The unit under test is installed into a large computer controlled rotary stage using the existing lens-to-camera threaded interface. The end-use dewar configuration features as specified in

Figure 3 are integrated into the interface plate behind the lens assembly, including the warm filter, a knife edge representing the cold stop, and the cold filter. This ensures that the measured performance of the lens represents how the lens will perform once it has been integrated with the customer's camera/dewar assembly.

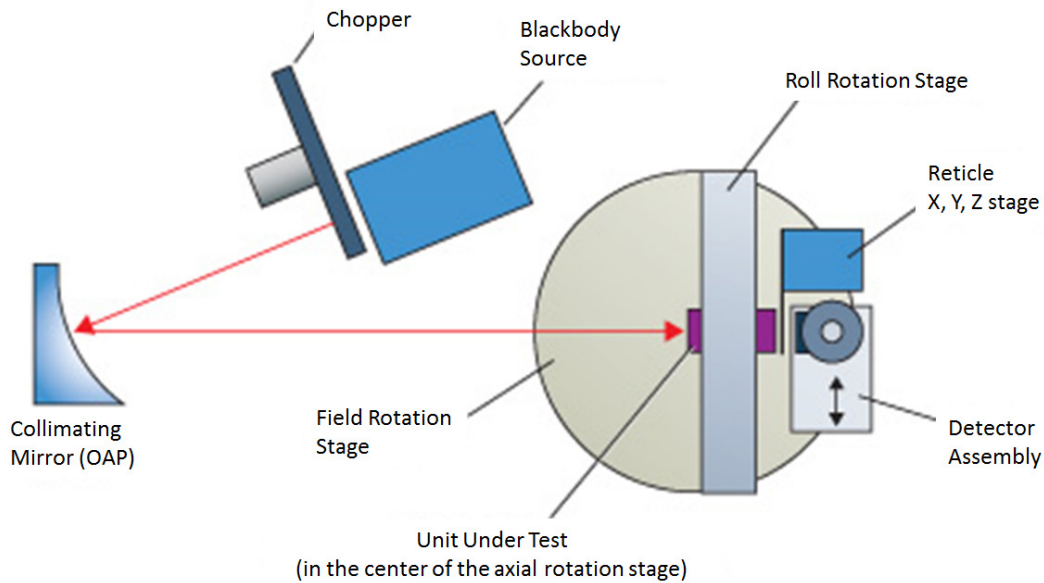


Figure 29: Basic Ensquared Energy Test Bench Components

Behind the lens assembly, the InSb detector is installed onto a 4-axis linear stage stack, allowing for precise computer controlled positioning of the detector relative to the lens. Between the lens assembly and the detector is a custom patterned reticle, consisting of specialized etched features on an AR-coated ZnSe substrate. The features include a 25 micron x 25 micron square, representing the size of a pixel, and a larger 250 micron x 250 micron square, referred to as the “world” aperture. These apertures are what allow for the direct measurement of Ensquared Energy within a 25 micron square pixel.

Both the large axial rotary stage holding the lens assembly and the InSb detector stage assembly are positioned on top of another large computer controlled rotary stage, serving as the

field rotational stage. This stage rotates the lens and detector relative to the incoming collimated wavefront, representing different object field angles. The entire 6-stage assembly allows for the complete manipulation of the unit under test. The unit under test, Detector Stage Assembly, axial rotational stage, and field rotational stage are shown in Figure 30 and Figure 31. Using this test bench, each lens is tested against the various performance requirements.

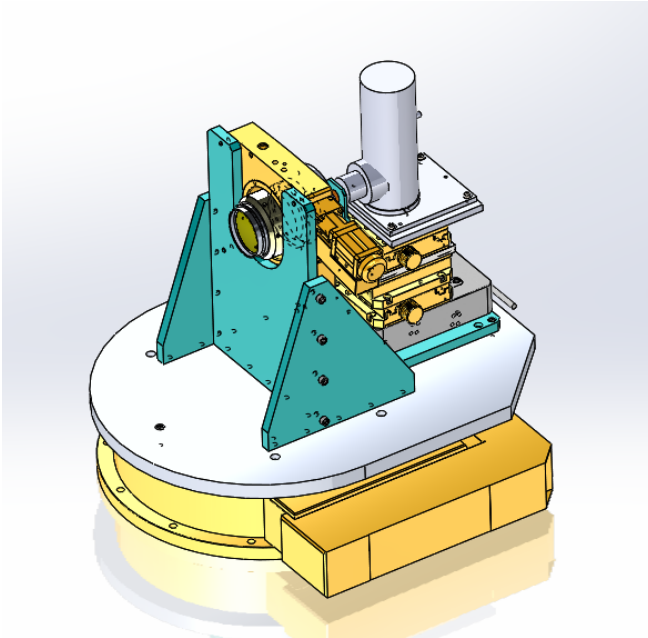


Figure 30: UUT and Detector Stage Assembly - Front

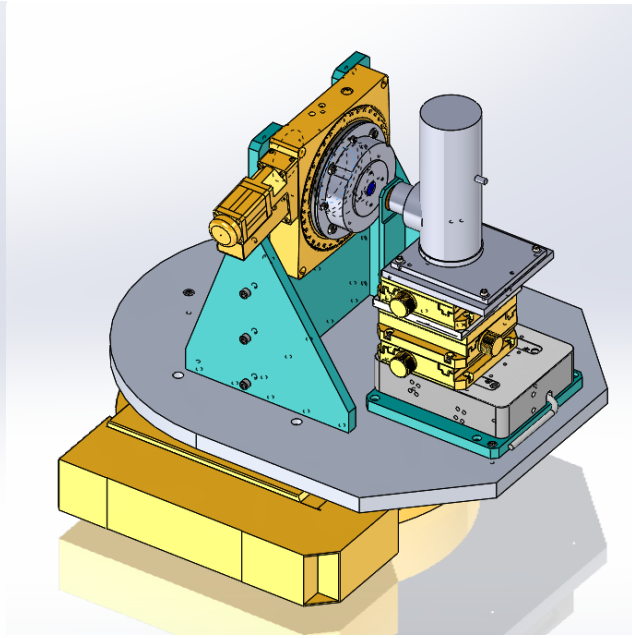


Figure 31: UUT and Detector Stage Assembly - Rear

### Performance Measurements

Measurements are made at 17 field points as defined in Figure 32. A set of 4 field points is measured for 4 different clocked orientations of the lens assembly, each separated by 90 degrees. The 4 field points in each set of measurements correspond to on-axis, the vertical (short) and horizontal (long) edges, and corner of the detector array. The 17<sup>th</sup> and final field point measured is 1 degree off-axis, and is measured when the lens is clocked at 0 degrees. This measurement is used for determining the paraxial focal length of the lens under test.

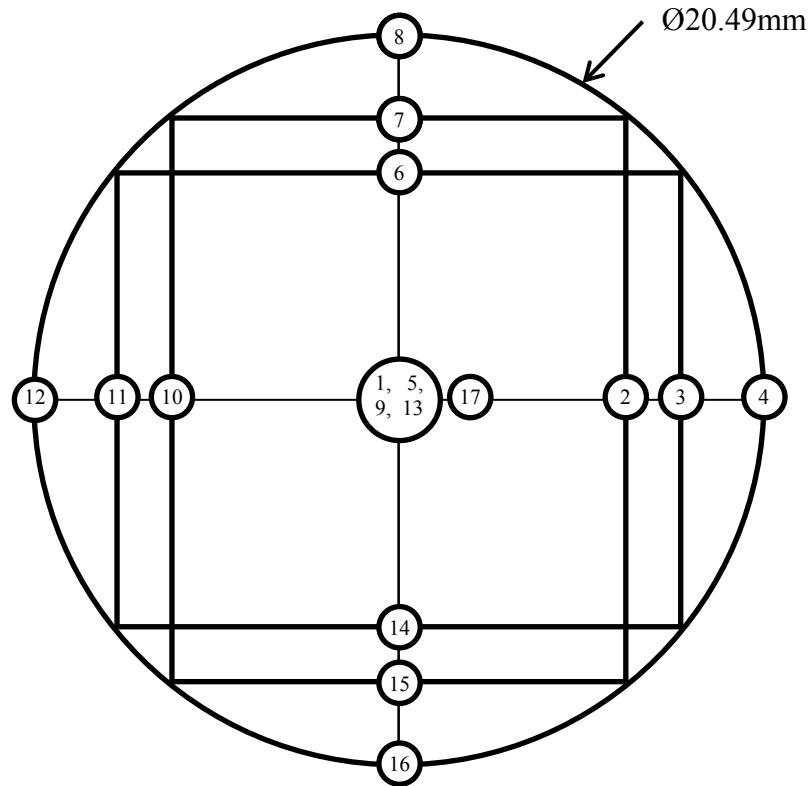


Figure 32: Test Field Points at Image Plane

Field Points 1, 5, 9, and 13 are the on-axis points and represent the origins of the image plane when the lens is clocked in four different positions.

Field Points 2, 6, 10, and 14 are located 6.4mm radially from the origin and represent the vertical (short) edge of the image plane.

Field Points 3, 7, 11, and 15 are located 8.0mm radially from the origin and represent the horizontal (long) edge of the image plane.

Field Points 4, 8, 12, and 16 are located 10.245mm radially from the origin and represent the corners of the image plane.

Field Point 17 is located 0.5mm off-axis

For each field point, the lens is clocked to the corresponding position, and the entire lens and detector assembly is rotated relative to the collimated wavefront to the angle corresponding to the image height of the field point. The reticle is positioned precisely in the focal plane of the Objective Lens Assembly and the InSb detector is directly behind the reticle to collect the energy that passes through the respective apertures of the reticle. At each of the 17 field points, the reticle is first moved so that the 250 micron square aperture is centered around the focused spot at the plane of focus, allowing the energy to pass and be collected by the detector. Then, the reticle is translated so that the 25 micron square aperture is centered around the focus spot,

allowing only energy that falls within the 25 micron square to be collected by the detector. Any energy that falls outside of the bounds of the 25 micron square is blocked by the opaque area of the precision reticle. This process is repeated as the reticle is moved axially through the plane of focus in 10 micron steps, creating a complete through focus measurement. The voltage from the InSb detector is captured with a Lock-In-Amplifier that is synchronized to the chopped blackbody source. Once the full test program is complete, the raw data is processed in a spreadsheet and the final results are calculated and presented as follows. The example test results shown below are actual results for a single tested objective lens assembly.

#### *Ensquared Energy*

The ratio of the voltages measured when the pixel aperture and then the world aperture are placed at the focused spot is calculated to determine the Ensquared Energy.

$$\textit{Ensquared Energy} = \frac{\textit{Pixel Voltage}}{\textit{World Voltage}}$$

Equation 4

Ensquared Energy measurements are made in three planes of focus, each separated by 10 microns. The Ensquared Energy results are reported for the single best plane of focus. Figure 33 shows the through focus Ensquared Energy test results for field points 1-16. The focus position is recorded as the position of the Z linear stage that positions the detector assembly, relative to its home position. In the presented example, the plane of best focus is at the focus position of -2.410 mm. Through focus Ensquared Energy curves are a useful diagnostic tool, from which many performance parameters can be determined, such as depth of focus, field curvature, and field tilt (Holloway & Weed, n.d.). With the exception of field point 8, all field points shown in **Figure 33** exhibit curves whose peaks are well centered with one another, indicating a flat plane of best focus across the full field. The curve for field point 8, which corresponds to an image height

representing a corner of the detector array, has a peak that is offset from the others by approximately 20 microns; however, the depth of focus over which the performance requirements are met is much larger than 20 microns.

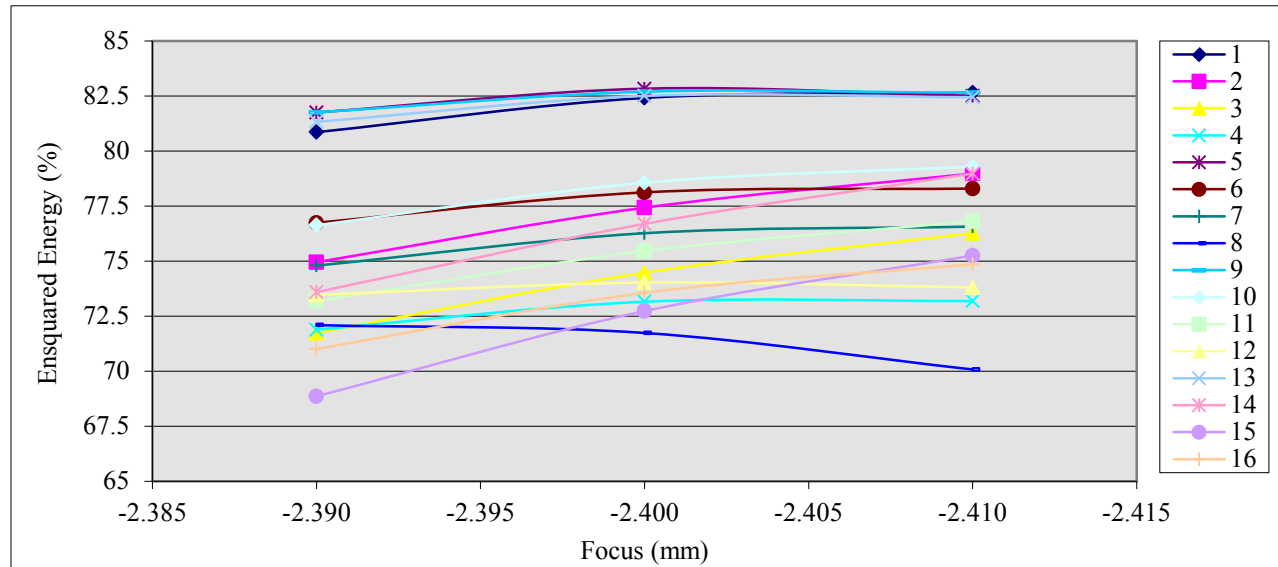


Figure 33: Through Focus Ensquared Energy Test Result

For every field point measurement, the Ensquared Energy, the world voltage, the pixel voltage, the object space field angle, the axial rotation angle, and the image height are all recorded. The data collected over the field is analyzed to determine the Field of View, Distortion, Relative Illumination, and the Boresight Accuracy.

#### *Field of View*

The field of view angle in object space is obtained through calculation using the calculated effective focal length at a specified image height, according to the following relation:

$$\text{Field Angle} = \tan^{-1} \left( \frac{\text{Image Height}}{\text{EFL}} \right)$$

Equation 5

The azimuth and elevation fields of view are calculated for image heights corresponding to the horizontal and vertical edges of the detector array, respectively. The example result in Figure 34

includes bold black lines indicating the bounds of the requirement, and error bars associated with the measurement resulting from the accuracy of the linear stages.

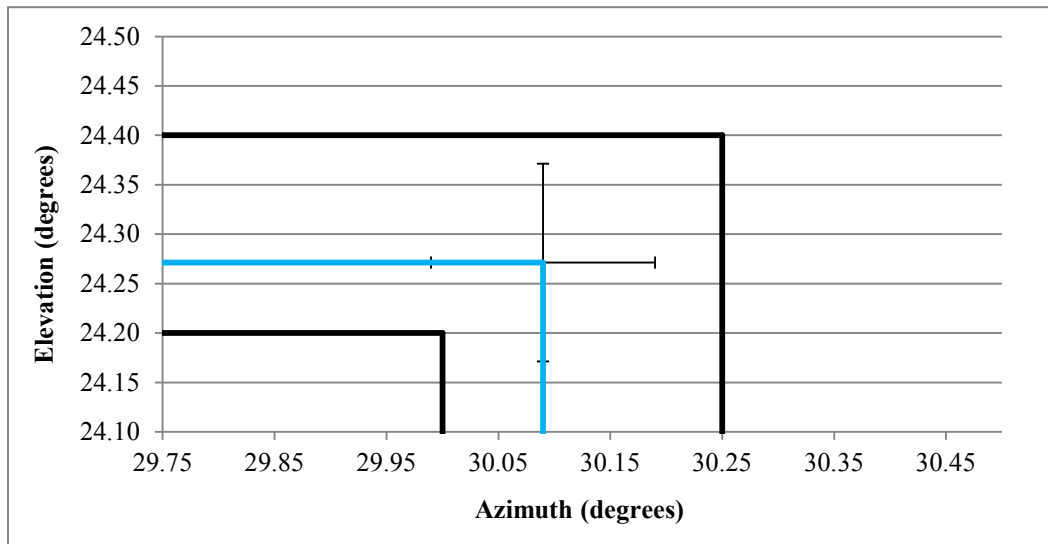


Figure 34: Field of View Test Result

### *Distortion*

To calculate distortion, the exact Effective Focal Length is calculated at each field point from the measured image height and field angle, defined as:

$$EFL = \frac{\text{Image Height}}{\tan(\text{Field Angle})}$$

Equation 6

Distortion at each field point is calculated as the ratio of the EFL at the off-axis field point to the on-axis EFL, and is reported as a percent. As the on-axis EFL cannot be obtained from an image height of 0, it is approximated from a measurement made at field point 17, which has a field angle of 1 degree.

$$\text{Distortion} = \frac{(\text{Field EFL} - \text{On Axis EFL})}{\text{On Axis EFL}} * 100\%$$

Equation 7

### *Relative Illumination*

The Relative Illumination of a field point is calculated as the ratio of the world voltage value at that off-axis field point to the on-axis world voltage value. A drop off in relative illumination with increasing field height is typical of optical systems that are non-telecentric in image space, and is caused by the increasing angle of incidence of the center ray of each field point on the image plane. An example Relative Illumination result is shown in Figure 35.

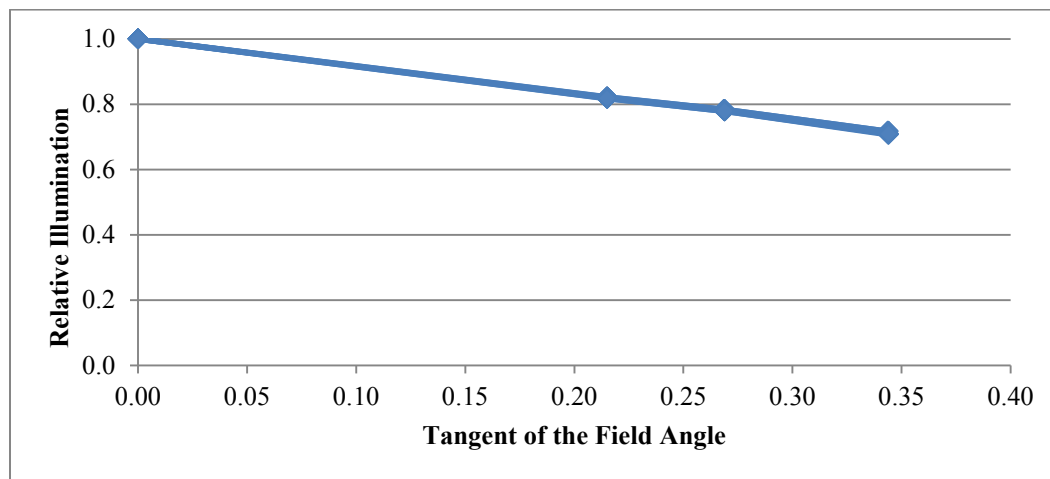


Figure 35: Relative Illumination Test Result

### *Boresight Accuracy*

As part of the calibration procedure of the test bench, the axis of the lens interface mount was aligned to the axial rotational stage axis to within 4 microns. The boresight accuracy, defined as the displacement between the optical and mechanical axes of the objective lens assembly, is verified by tracking the position of the focused on-axis spot as the lens is rotated about its mechanical axis in 90 degree increments. The radius of the circle traced by the positions of the spots represents the boresight error of the system. Figure 36 shows the positions of the four on-axis focused spots representing field points, 1, 5, 9, and 13. The X and Y positions of the spot are recorded as the positions of the X and Y linear stages that control the motion of the detector

assembly, relative to their home positions. For the example shown, the circle traced by the four spots has a radius of 42 microns, representing a boresight accuracy of the same value.

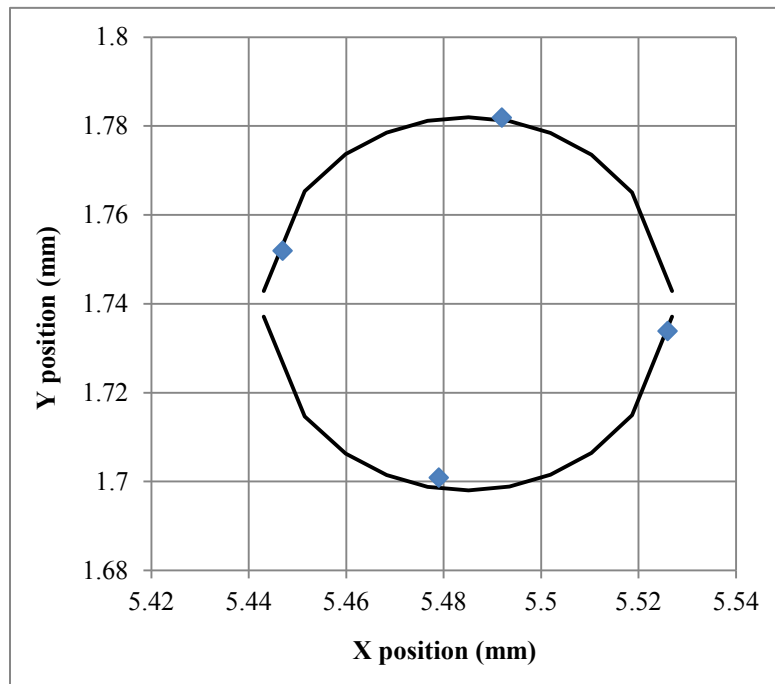


Figure 36: Boresight Test Result

At the time of this writing, a total of 39 out of 41 objective lens assemblies had been assembled and tested. The test results of these 39 objective lens assemblies are summarized in Table 7. The maximum and minimum values of each test result are reported, in addition to the average test result for each parameter. The average results compare quite well to the nominal design values. For instance, the average measured effective focal length and field of view for all units is within 0.2% of the nominal design value. The Ensquared Energy results are within 13% of the nominal design values, and the Relative Illumination result is within 4% of the nominal design value. Regarding distortion, the percent error of the average measured value compared with the design nominal value is high due to the very small value. However, it should be noted that the average value is approximately 7x under the requirement value of 2%.

Parameter	Design Value	As-Built Test Result of 39 Assemblies		
		Max Value	Min Value	Average Value
EFL	29.77 mm	29.875 mm	29.647 mm	29.724 mm
Field of View	30.102 degrees Az x 24.279 degrees El	30.203 degrees Az x 24.364 degrees El	29.982 degrees Az x 24.183 degrees El	30.131 degrees Az x 24.305 degrees El
Ensquared Energy at Lowest Field Point within $\pm 6.4$ mm off-axis	85.6%	78.2%	69.5%	74.5%
Ensquared Energy at Lowest Corner Field Point	77.7%	73.3%	61.9%	67.8%
Distortion	.079% uncorrected	0.80%	0.10%	0.29%
Relative Illumination	73.5%	71.3%	69.2%	70.5%
Boresight Accuracy	<100 $\mu\text{m}$	80.0 $\mu\text{m}$	5.5 $\mu\text{m}$	39.9 $\mu\text{m}$

Table 7: Summary of Test Results for 39 Assemblies

## CONCLUSION

The design and full specification of a custom high performance SWIR/MIWR objective lens assembly has been thoroughly described, with an emphasis on considerations for manufacturing and producibility. The approach, strategies, and tools used to execute the design have been discussed, including the preparation and organization of a complete “Table 1” reference.

Fabrication and metrology methods for the optical elements were presented, ranging from the time tested and proven conventional polishing method, to the next generation and highly accurate single point diamond turning method. Assembly and test processes were defined and executed with high yield and success, resulting in the completion of 41 compliant objective lens assemblies. Finally, average test results of the entire lot were presented and compared against the design predictions, showing a high degree of correlation.

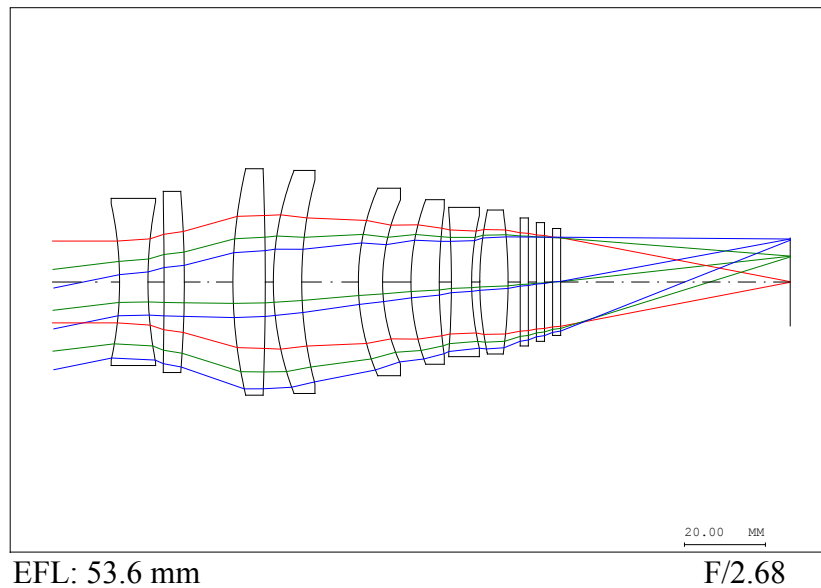
There is nothing more satisfying for an engineer than to have his design realized as built hardware. Many designs may never achieve this status for various reasons, which makes it even more special for the select designs that do. A strong sense of accomplishment and pride is most certainly experienced as one witnesses the progression of his design through the succession of developmental gates and into production.



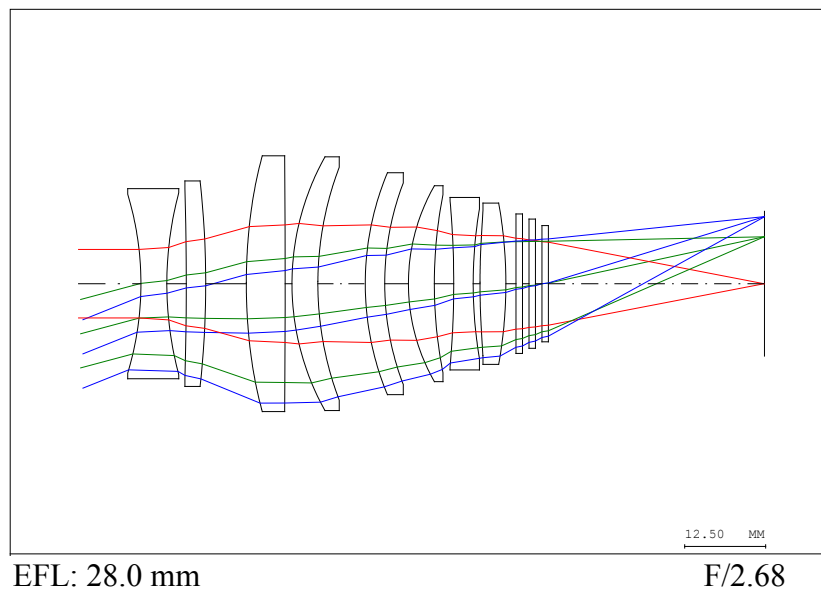
Figure 37: High Resolution Photograph of F/2 Broadband Infrared High Performance Objective Lens Assembly

## APPENDIX A: EVOLUTION OF THE OPTICAL DESIGN

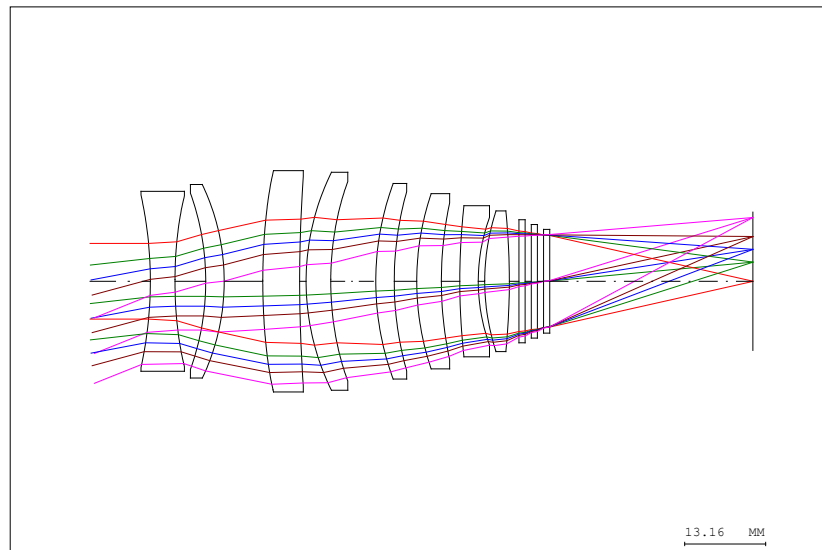
The following is intended to depict and briefly describe the evolution of the optical design of the SWIR/MWIR Objective Lens Assembly from a selected starting point design to a refined and complete final design.



Starting Point Design: 8 Elements



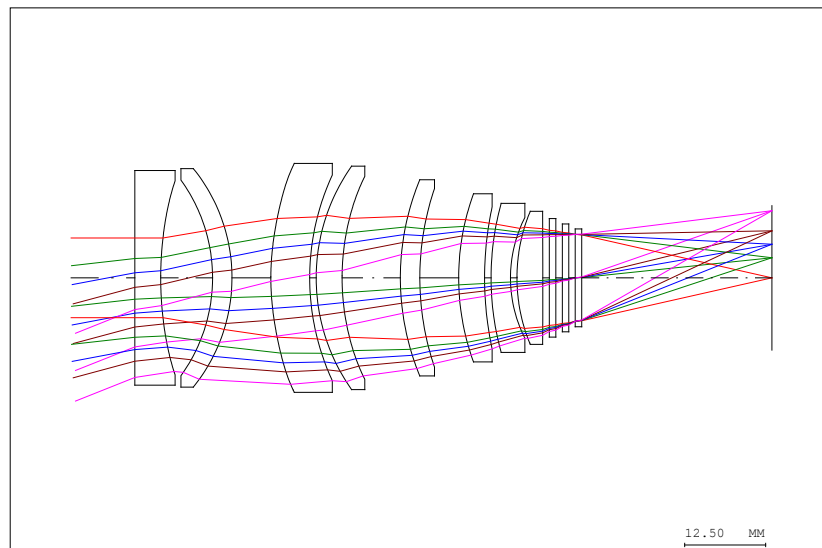
Starting Point Design scaled to 28.0 mm EFL



EFL: 28.0 mm

F/2.30

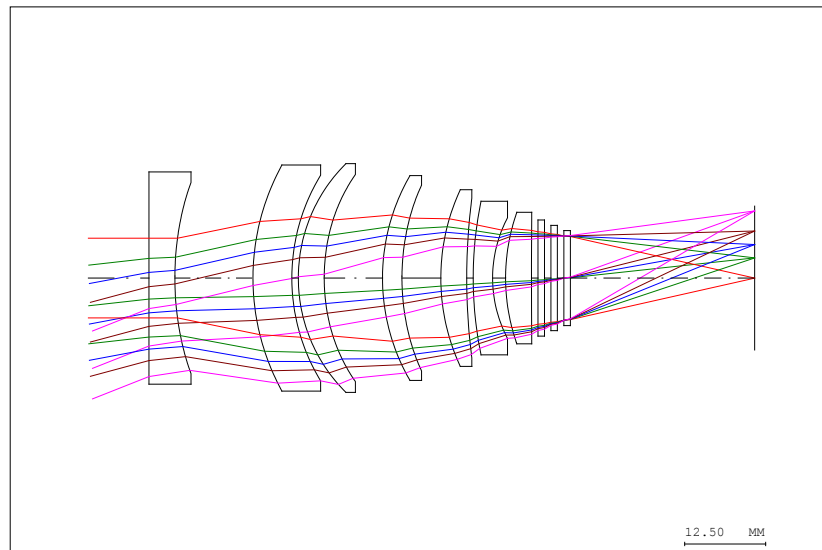
Set the Image Plane Size, decreasing F/#



EFL: 28.0 mm

F/2.30

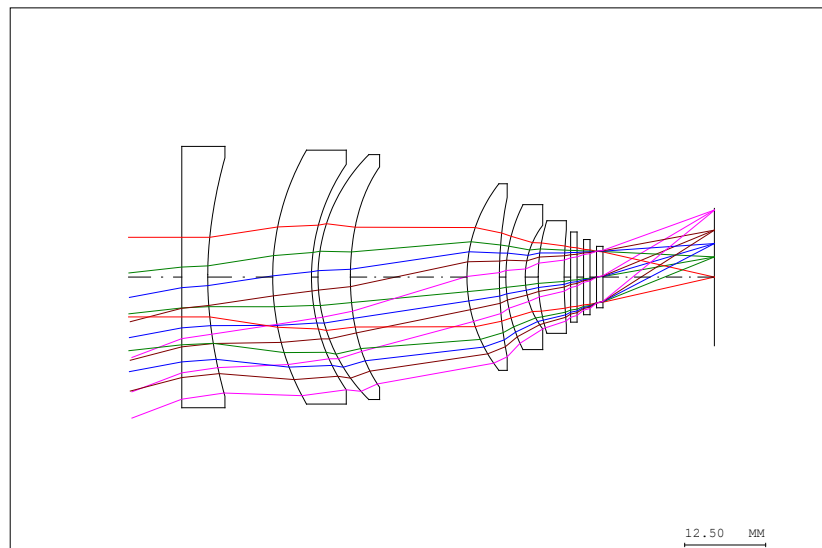
Continued Optimization  
Element 2 is driving towards a “shell” with little power



EFL: 28.0 mm

F/2.30

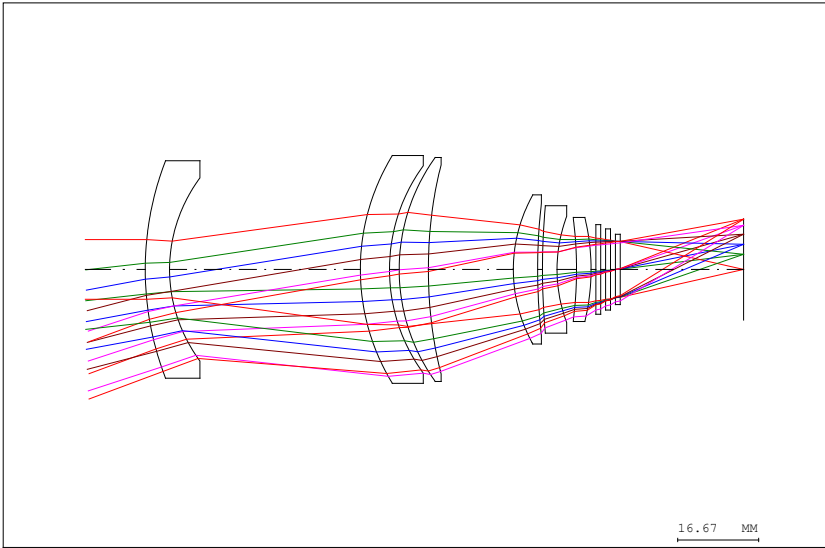
Element 2 removed, optimization continued



EFL: 28.0 mm

F/2.30

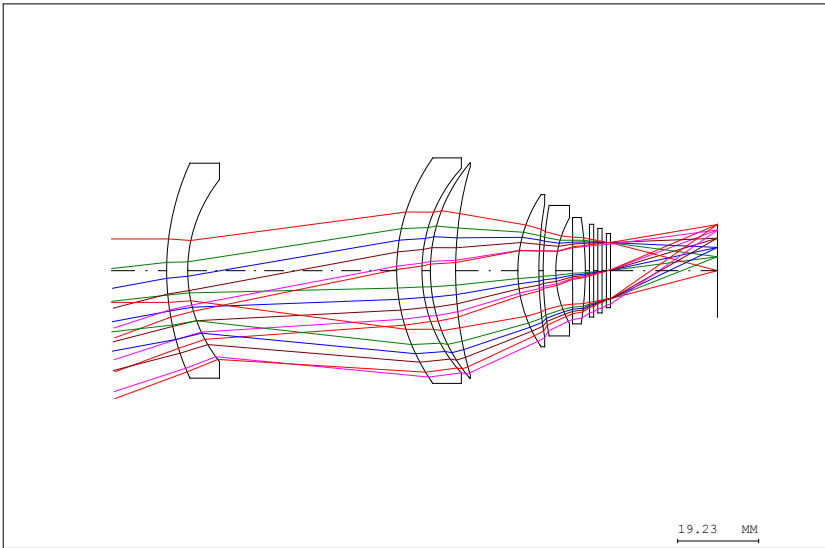
Element 4 removed, optimization continued  
Cold Stop to Image Plane distance set to specified value



EFL: 28.0 mm

F/2.30

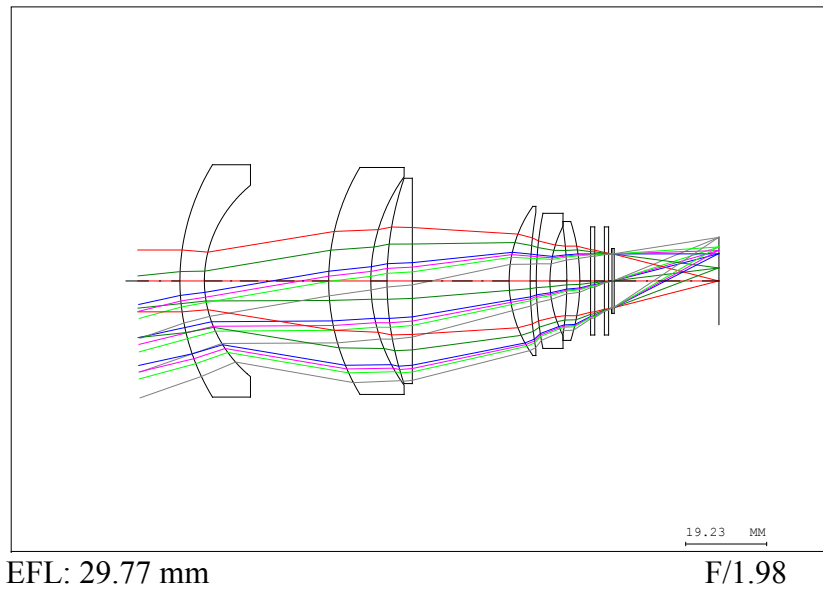
Further optimization for improved performance



EFL: 29.86 mm

F/2.0

Further optimization to decrease F/#



**Final Design**  
Second surface of Element 3 set to plano, and system re-optimized  
Overall length reduced

APPENDIX B: PARAXIAL RAY TRACE AND ABERRATION THEORY

Surface	Element 1		Element 2		Element 3		Element 4		Element 5		Element 6		Warm Filter		Dewar Window		Stop		Cold Filter		Image
	0	1	2	3	4	5	6	7	8	9	10	11	12	13	14	15	16	17	18	19	
R	-	52.096987	27.732967	51.620969	41.932678	73.971385	1E+18	30.092749	96.879893	80.676517	28.168249	-105.27452	-46.193265	1E+18	1E+18	1E+18	1E+18	1E+18	1E+18	1E+18	1E+18
C	-	0.019195	0.036058	0.019372	0.023848	0.013519	0.000000	0.033231	0.010322	0.012395	0.035501	-0.009499	-0.021648	0.000000	0.000000	0.000000	0.000000	0.000000	0.000000	0.000000	0.000000
A <sub>s</sub> Asphere Coefficient			-7.212E-07																		
t			5.8	29.534867	10	3.8573919	6	23.001943	5	1.4439239	3.25	3.9998994	3.1	2.55	1	2.286	1	0.7112	0.1016	0.5	24.89962
Material	Air	ZnSe	Air	CaF2	Air	ZnSe	Air	ZnSe	Air	IG-3	Air	ZnSe	Air	ZnS	Air	Sapphire	Air	Air	Air	ZnS	Air
n <sub>2800nm</sub>	1	2.438753	1	1.419220	1	2.438753	1	2.438753	1	2.813581	1	2.438753	1	2.258359	1	1.718167	1	1	1	2.258359	1
n <sub>1300nm</sub>	1	2.465510	1	1.427213	1	2.465510	1	2.465510	1	2.889354	1	2.465510	1	2.27748	1	1.750481	1	1	1	2.27748	1
n <sub>950nm</sub>	1	2.433332	1	1.410112	1	2.433332	1	2.433332	1	2.803736	1	2.433332	1	2.252053	1	1.677405	1	1	1	2.252053	1

-Φ	0	-0.027617	0.051879	-0.008121	0.009997	-0.019450	0.000000	-0.047811	0.014851	-0.022480	0.064384	0.013667	-0.031146	0.000000	0.000000	0.000000	0.000000	0.000000	0.000000	0.000000	0.000000	0.000000
t/n	0	2.378265	29.534867	7.046124	3.857392	2.460274	23.001943	2.050228	1.443924	1.155112	3.999899	1.271141	2.550000	0.442799	2.286000	0.582016	0.711200	0.101600	0.221400	24.899620		

y <sub>p</sub>	1	1	0.9343199	1.550257	1.6084915	1.7024019	1.6808342	1.4791909	1.3162236	1.2296743	1.1285062	1.0688063	1.0684016	0.9827339	0.967858	0.8910594	0.8715065	0.8476136	0.8442004	0.8367624	0.0002553
nu <sub>p</sub>	0	-0.0276168	0.0208546	0.0082648	0.0243456	-0.0087664	-0.0087664	-0.0794874	-0.0599403	-0.087583	-0.0149254	-0.0003183	-0.0335952	-0.0335952	-0.0335952	-0.0335952	-0.0335952	-0.0335952	-0.0335952	-0.0335952	-0.0335952
u <sub>p</sub>	0	-0.0113242	0.0208546	0.0058234	0.0243456	-0.0035946	-0.0087664	-0.0325935	-0.0599403	-0.0311286	-0.0149254	-0.0001305	-0.0335952	-0.0148759	-0.0335952	-0.0195529	-0.0335952	-0.0335952	-0.0335952	-0.0148759	-0.0335952

y	7.5	7.5	7.0073992	11.626927	12.063686	12.768014	12.606257	11.093931	9.8716767	9.2225574	8.4637967	8.0160471	8.0130122	7.3705045	7.2589351	6.6829458	6.5362989	6.3571023	6.3315027	6.275718	0.0019148
nu	0	-0.2071261	0.1564093	0.0619857	0.1825918	-0.0657477	-0.0657477	-0.5961555	-0.4495522	-0.6568722	-0.1119402	-0.0023875	-0.2519638	-0.2519638	-0.2519638	-0.2519638	-0.2519638	-0.2519638	-0.2519638	-0.2519638	-0.2519638
u	0	-0.0849312	0.1564093	0.0436759	0.1825918	-0.0269596	-0.0657477	-0.2444509	-0.4495522	-0.2334648	-0.1119402	-0.000979	-0.2519638	-0.1115694	-0.2519638	-0.1466469	-0.2519638	-0.2519638	-0.1115694	-0.2519638	

$\bar{y}$	0	-18.218036	-16.18417	-15.724196	-14.714684	-14.729487	-14.034083	-7.5325142	-6.2146538	-5.4197823	-4.6431674	-3.1496697	-2.729763	-1.6705937	-1.4866723	-0.5371581	-0.2954118	-7.404E-06	0.0421932	0.1341539	10.476473
$\bar{nu}$	0.352065	0.8551892	0.0155739	0.143272	-0.0038374	0.282653	0.282653	0.6427872	0.550494	0.6723289	0.3733838	0.3303383	0.4153605	0.4153605	0.4153605	0.4153605	0.4153605	0.4153605	0.4153605	0.4153605	0.4153605
$\bar{u}$	0.352065	0.3506666	0.0155739	0.1009512	-0.0038374	0.1159006	0.282653	0.2635721	0.550494	0.2389584	0.3733838	0.1354538	0.4153605	0.1839214	0.4153605	0.2417463	0.4153605	0.4153605	0.1839214	0.4153605	

LI	-	2.6404875	2.6404875	2.6404875	2.6404875	2.6404875	2.6404875	2.6404875	2.6404875	2.6404875	2.6404875	2.6404875	2.6404875	2.6404875	2.6404875	2.6404875	2.6404875	2.6404875	2.6404875	2.6404875	2.6404875
----	---	-----------	-----------	-----------	-----------	-----------	-----------	-----------	-----------	-----------	-----------	-----------	-----------	-----------	-----------	-----------	-----------	-----------	-----------	-----------	-----------

Surface	0	1	2	3	4	5	6	7	8	9	10	11	12	13	14	15	16	17	18	19
A		0.1439623	0.4090833	0.3816458	0.4702836	0.3551993	-0.0657477	0.3029102	-0.3476562	-0.335237	0.1885327	-0.1880844	-0.4254309	-0.2519638	-0.2519638	-0.2519638	-0.2519638	-0.2519638	-0.2519638	-0.2519638
$\bar{A}$		0.0023704	-0.5679976	-0.2890348	-0.3547495	-0.2029615	0.282653	0.0323431	0.486346	0.4833148	0.2085469	0.4033024	0.4744549	0.4153605	0.4153605	0.4153605	0.4153605	0.4153605	0.4153605	0.4153605
$\Delta(\frac{u}{n})$		-0.0348257	0.191235	-0.1256348	0.1518172	-0.1936465	-0.0546931	-0.0344883	-0.3493162	0.3665744	-0.0289624	0.1115388	-0.2515624	0.2025609	-0.2025609	0.166613	-0.166613	0	0.2025609	-0.2025609
$\Delta(\frac{1}{n})$		-0.5899544	0.5899544	-0.2953876	0.2953876	-0.5899544	0.5899544	-0.5899544	0.5899544	-0.6445811	0.6445811	-0.5899544	0.5899544	-0.5572006	0.5572006	-0.4179844	0.4179844	0	-0.5572006	0.5572006

Chromatic Coefficients

Surface	0	1	2	3	4	5	6	7	8	9	10	11	12	13	14	15	16	17	18	19		
$\partial_\lambda W_{020}$		0.0071231	-0.0189117	0.0267342	-0.0341808	0.0299197	0.005468	0.0221697	0.0226413	-0.0470413	-0.0242788	-0.0099466	0.0224898	-0.0104546	0.0102963	-0.0358084	0.0350227	0	-0.0089808	0.0089017	Sum	0.0011637
$\partial_\lambda W_{111}$		0.0002346	0.0525164	-0.0404936	0.0515672	-0.0341923	-0.0470144	0.0047343	-0.0633472	0.1356398	-0.0537124	0.0426562	-0.0501628	0.0344687	-0.0339469	0.1180599	-0.1154693	0	0.0296097	-0.0293488	Sum	0.001799

**A<sub>4</sub> Asphere Coefficient Contributions**

Surface	0	1	2	3	4	5	6	7	8	9	10	11	12	13	14	15	16	17	18	19	Contribution Sums		
a		0	0.0200149	0	0	0	0	0	0	0	0	-0.335921	0	0	0	0	0	0	0	0	0		
$\delta S1$		0	0.0200149	0	0	0	0	0	0	0	0	-0.335921	0	0	0	0	0	0	0	0	0	$\delta S1$	-0.315906
$\delta S2$		0	-0.0462261	0	0	0	0	0	0	0	0	0.1319903	0	0	0	0	0	0	0	0	0	$\delta S2$	0.0857641
$\delta S3$		0	0.1067631	0	0	0	0	0	0	0	0	-0.0518617	0	0	0	0	0	0	0	0	0	$\delta S3$	0.0549014
$\delta S4$		0	0	0	0	0	0	0	0	0	0	0	0	0	0	0	0	0	0	0	0	$\delta S4$	0
$\delta S5$		0	-0.2465783	0	0	0	0	0	0	0	0	0.0203775	0	0	0	0	0	0	0	0	0	$\delta S5$	-0.2262008
$\partial_\lambda W_{020}$		0	0	0	0	0	0	0	0	0	0	0	0	0	0	0	0	0	0	0	0	$\partial_\lambda W_{020}$	0
$\partial_\lambda W_{111}$		0	0	0	0	0	0	0	0	0	0	0	0	0	0	0	0	0	0	0	0	$\partial_\lambda W_{111}$	0

**Seidel Terms**

																								Seidel Sums
<b>S1</b>		0.0054132	-0.2242578	0.2127629	-0.4050613	0.3119443	0.0029804	0.0351063	0.4167827	-0.379942	0.0087131	-0.0316295	0.3648376	-0.0947827	0.093348	-0.0706892	0.0691381	0	-0.0814215	0.0807041	<b>S1</b>	<b>0.3139466</b>		
<b>S2</b>		8.913E-05	0.311374	-0.1611333	0.3055503	-0.1782455	-0.0128131	0.0037485	-0.5830489	0.5477666	0.0096381	0.0678219	-0.4068792	0.1562487	-0.1538835	0.1165307	-0.1139736	0	0.1342227	-0.1330401	<b>S2</b>	<b>-0.0900267</b>		
<b>S3</b>		1.468E-06	-0.4323318	0.1220324	-0.2304861	0.1018498	0.055084	0.0004002	0.8156435	-0.7897212	0.0106612	-0.145428	0.4537655	-0.2575748	0.2536758	-0.1921	0.1878847	0	-0.2212651	0.2193156	<b>S3</b>	<b>-0.0485928</b>		
<b>S4</b>		0.078954	-0.1483168	0.0398965	-0.0491143	0.0556062	-4.113E-18	0.1366862	-0.0424574	0.0557056	-0.159546	-0.0390718	0.0890447	3.885E-18	-3.885E-18	2.914E-18	-2.914E-18	0	3.885E-18	-3.885E-18	<b>S4</b>	<b>0.0173869</b>		
<b>S5</b>		0.0013	0.8062099	-0.1226348	0.2109113	-0.0899706	-0.2368092	0.0146373	-1.0816317	1.0582384	-0.16469	0.3956159	-0.6053602	0.4246102	-0.4181828	0.3166755	-0.3097265	0	0.364754	-0.3615402	<b>S5</b>	<b>0.2024065</b>		

$\lambda$ [mm] 2.800000E-03

Raytrace Results

	mm	waves		
S1	-0.0019594	-0.6997979	<b>W<sub>040</sub></b>	<b>-0.0874747</b>
S2	-0.0042626	-1.5223496	<b>W<sub>131</sub></b>	<b>-0.7611748</b>
S3	0.0063086	2.2530866	<b>W<sub>222</sub></b>	<b>1.1265433</b>
S4	0.0173869	6.2095922	<b>W<sub>220</sub></b>	<b>2.1156697</b>
S5	-0.0237943	-8.4979644	<b>W<sub>311</sub></b>	<b>-4.2489822</b>
			$\partial_\lambda W_{020}$	<b>0.0011637</b>
			$\partial_\lambda W_{111}$	<b>0.001799</b>

Code V Results

$\lambda$ [mm] 2.800000E-03

	waves	mm		
W <sub>040</sub>	-0.0875	-0.000245	<b>S1</b>	<b>-0.00196</b>
W <sub>131</sub>	-0.7611	-0.0021311	<b>S2</b>	<b>-0.0042622</b>
W <sub>222</sub>	1.1264	0.0031539	<b>S3</b>	<b>0.0063078</b>
W <sub>220</sub>	2.1156	0.0059237	<b>S4</b>	<b>0.0173869</b>
W <sub>311</sub>	-4.2489	-0.0118969	<b>S5</b>	<b>-0.0237938</b>

Accuracy of Ray Trace to Code V Results

-0.0289%
0.0098%
0.0127%
-0.0001%
0.0019%

Seidel aberration contributions from only the A<sub>4</sub> asphere coefficients are determined in this aberration theory study, although the two aspheric surfaces include A<sub>6</sub> and A<sub>8</sub> asphere coefficients as well.

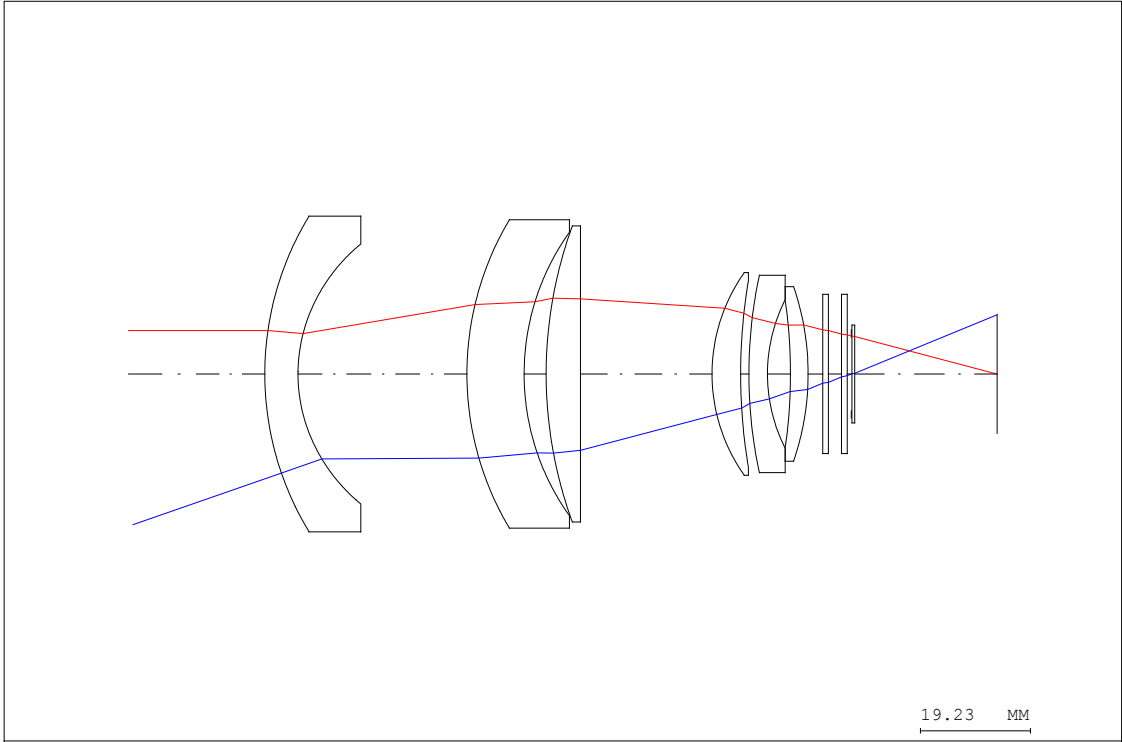


Figure 38: Marginal (Red) and Chief (Blue) Rays

## APPENDIX C: TOLERANCE SENSITIVITIES

The following presents the individual sensitivities to overall RMS wavefront error of the full set of tolerances assigned to the system. For brevity, only the full data for the on-axis field are presented, however the overall impact of the tolerances to performance for all fields is presented at the end.

NOTE - All tolerances are listed.

115 tolerances and compensators have been used

This system is symmetric. In the compensation calculations the opposite side of the field will be simulated

Execution time is proportional to the product of the number of fields and number of wavelengths. You can reduce your execution time by reducing these numbers accordingly.

Estimated relative execution time = 54

CODE V                      POSITION 1

SENSITIVITY ANALYSIS  
POLYCHROMATIC RMS WAVEFRONT ABERRATION

-----  
FIELD (X,Y) = ( 0.00, 0.00)MAX, ( 0.00, 0.00)DEG  
FIELD WEIGHT =  
1.00

WAVELENGTH	WEIGHT	NO. OF RAYS
3950.0 NM	202	772
3500.0 NM	203	772
2800.0 NM	176	772
2000.0 NM	86	772
1300.0 NM	10	772

NOMINAL RMS            = 0.0948  
-----

MANUFACTURING ERROR		CHANGES IN RMS FOR PLUS AND MINUS MANUFACTURING ERRORS		COMPENSATING PARAMTERES DLT S13	
TYPE		CHANGE			
DLF	S2	2.0000000v	0.0000	0.0000	-0.001999
DLF	S3	2.0000000v	0.0006	-0.0006	0.002590
DLF	S4	2.0000000v	-0.0003	0.0003	-0.001866
DLF	S5	2.0000000v	0.0006	-0.0006	0.002529
DLF	S6	2.0000000v	-0.0005	0.0006	-0.008760
DLF	S7	2.0000000v	0.0004	-0.0004	0.008990
DLF	S8	2.0000000v	-0.0008	0.0009	-0.011899
DLF	S9	2.0000000v	0.0023	-0.0021	0.013428
DLF	S10	2.0000000v	-0.0019	0.0020	-0.014754
DLF	S11	2.0000000v	0.0014	-0.0013	0.016855
DLF	S12	2.0000000v	-0.0024	0.0026	-0.014252
DLF	S13	2.0000000v	0.0025	-0.0023	0.011919
DLT	S2	0.0250000v	0.0001	-0.0001	-0.006872
DLT	S3	0.0400000v	-0.0023	0.0026	-0.018573
DLT	S4	0.0500000v	0.0002	-0.0002	-0.001933
DLT	S5	0.0250000v	-0.0029	0.0034	-0.017299
DLT	S6	0.0250000v	0.0015	-0.0014	0.000084
DLT	S7	0.0250000v	0.0038	-0.0035	0.000212
DLT	S8	0.0250000v	0.0009	-0.0006	-0.062132
DLT	S9	0.0250000v	0.0013	-0.0004	-0.087401
DLT	S10	0.0250000v	0.0004	-0.0001	-0.065602
DLT	S11	0.0250000v	0.0061	-0.0053	-0.002383
DLT	S12	0.0250000v	0.0033	-0.0031	0.001525
DLT	S13	0.0250000v	0.0000	0.0000	-0.025000
DLN	S2	0.0010000v	-0.0005	0.0005	0.011097
DLN	S4	0.0010000v	0.0029	-0.0026	0.016565
DLN	S6	0.0010000v	-0.0010	0.0010	-0.036753
DLN	S8	0.0010000v	-0.0044	0.0054	-0.050294
DLN	S10	0.0010000v	0.0028	-0.0025	0.029682
DLN	S12	0.0010000v	-0.0023	0.0025	-0.013862
CYD	S2	1.0000000v	0.0000	0.0000	-0.000495
CYD	S3	1.0000000v	0.0002	-0.0001	0.000627
CYD	S4	1.0000000v	-0.0001	0.0001	-0.000461
CYD	S5	1.0000000v	0.0002	-0.0001	0.000621
CYD	S6	1.0000000v	0.0005	0.0007	-0.002179
CYD	S7	1.0000000v	0.0008	0.0006	0.002248
CYD	S8	1.0000000v	0.0009	0.0013	-0.002928
CYD	S9	1.0000000v	0.0018	0.0007	0.003353
CYD	S10	1.0000000v	0.0011	0.0020	-0.003683
CYD	S11	1.0000000v	0.0025	0.0019	0.004176
CYD	S12	1.0000000v	0.0008	0.0020	-0.003561
CYD	S13	1.0000000v	0.0015	0.0003	0.002972

CYN	S2	1.0000000v	0.0002	-0.0001	-0.000410
CYN	S3	1.0000000v	0.0001	0.0000	0.000598
CYN	S4	1.0000000v	0.0000	0.0001	-0.000456
CYN	S5	1.0000000v	0.0002	-0.0001	0.000641
CYN	S6	1.0000000v	0.0008	0.0004	-0.002007
CYN	S7	1.0000000v	0.0003	0.0010	0.002025
CYN	S8	1.0000000v	0.0014	0.0008	-0.002669
CYN	S9	1.0000000v	0.0015	0.0010	0.003201
CYN	S10	1.0000000v	0.0015	0.0016	-0.003461
CYN	S11	1.0000000v	0.0018	0.0026	0.003799
CYN	S12	1.0000000v	0.0011	0.0017	-0.003417
CYN	S13	1.0000000v	0.0014	0.0005	0.002901
TRY	S2	0.0250000v	0.0003	0.0003	0.000000
TRX	S2	0.0250000v	0.0003	0.0003	0.000000
BTY	S2..3	0.0005000v	0.0003	0.0003	0.000000
BTX	S2..3	0.0005000v	0.0003	0.0003	0.000000
DSY	S2..3	0.0250000v	0.0007	0.0007	0.000000
DSX	S2..3	0.0250000v	0.0007	0.0007	0.000000
TRY	S4	0.0076000v	0.0001	0.0001	0.000000
TRX	S4	0.0076000v	0.0001	0.0001	0.000000
BTY	S4..5	0.0005000v	0.0004	0.0004	0.000000
BTX	S4..5	0.0005000v	0.0004	0.0004	0.000000
DSY	S4..5	0.0250000v	0.0004	0.0004	0.000000
DSX	S4..5	0.0250000v	0.0004	0.0004	0.000000
TRY	S6	0.0050000v	0.0002	0.0002	0.000000
TRX	S6	0.0050000v	0.0002	0.0002	0.000000
BTY	S6..7	0.0005000v	0.0007	0.0007	0.000000
BTX	S6..7	0.0005000v	0.0007	0.0007	0.000000
DSY	S6..7	0.0150000v	0.0008	0.0008	0.000000
DSX	S6..7	0.0150000v	0.0008	0.0008	0.000000
TRY	S8	0.0250000v	0.0046	0.0046	0.000000
TRX	S8	0.0250000v	0.0046	0.0046	0.000000
BTY	S8..9	0.0005000v	0.0012	0.0012	0.000000
BTX	S8..9	0.0005000v	0.0012	0.0012	0.000000
DSY	S8..9	0.0250000v	0.0020	0.0020	0.000000
DSX	S8..9	0.0250000v	0.0020	0.0020	0.000000
TRY	S10	0.0050000v	0.0009	0.0009	0.000000
TRX	S10	0.0050000v	0.0009	0.0009	0.000000
BTY	S10..11	0.0005000v	0.0014	0.0014	0.000000
BTX	S10..11	0.0005000v	0.0014	0.0014	0.000000
DSY	S10..11	0.0250000v	0.0040	0.0040	0.000000
DSX	S10..11	0.0250000v	0.0040	0.0040	0.000000
TRY	S12	0.0050000v	0.0003	0.0003	0.000000
TRX	S12	0.0050000v	0.0003	0.0003	0.000000
BTY	S12..13	0.0005000v	0.0003	0.0003	0.000000
BTX	S12..13	0.0005000v	0.0003	0.0003	0.000000

DSY	S12..13	0.0250000v	0.0003	0.0003	0.000000
DSX	S12..13	0.0250000v	0.0003	0.0003	0.000000
HOM	S2	0.5000E-05v	-0.0015	0.0017	0.000580
HOM	S4	0.0000300v	-0.0056	0.0246	0.008487
HOM	S6	0.5000E-05v	-0.0013	0.0016	0.000231
HOM	S8	0.5000E-05v	-0.0001	0.0002	0.000601
HOM	S10	0.0000300v	0.0012	-0.0003	0.009312
HOM	S12	0.5000E-05v	0.0002	-0.0002	0.000457
DLX	S12	0.0020320v	0.0000	0.0000	0.000000
DLY	S12	0.0020320v	0.0000	0.0000	0.000000
RPA	S2	0.0187290v	0.0000	0.0000	0.000039
RPA	S3	0.0319833v	0.0000	0.0000	-0.000065
RPA	S4	0.2057801v	0.0000	0.0000	0.000261
RPA	S5	0.0901218v	0.0000	0.0000	-0.000122
RPA	S6	0.0245238v	0.0000	0.0000	0.000141
RPA	S7	0.0247662v	0.0000	0.0000	-0.000155
RPA	S8	0.0424681v	0.0000	0.0000	0.000446
RPA	S9	0.0270701v	0.0000	0.0000	-0.000249
RPA	S10	0.0322565v	0.0000	0.0000	0.000408
RPA	S11	0.0379483v	0.0000	0.0000	-0.000558
RPA	S12	0.0630584v	0.0001	-0.0001	0.000710
RPA	S13	0.0472907v	-0.0001	0.0001	-0.000538
DLX	S3	0.0020000v	0.0000	0.0000	0.000000
DLY	S3	0.0020320v	0.0000	0.0000	0.000000
BTX	S2..13	0.0019000v	0.0000	0.0000	0.000000
BTY	S2..13	0.0019000v	0.0000	0.0000	0.000000

PROBABLE CHANGE IN RMS      0.0399

PROBABLE CHANGE OF COMPENSATORS (+/-)      0.179287

Units - linear dimensions in mm.    angles in radians,  
fringes in wavelengths at 632.8 nm.  
RMS is in wavelengths at 2387.9 nm.

The probable change and cumulative probability results are based on the assumption that the distribution of the RMS converges to a Gaussian form

CUMULATIVE PROBABILITY	CHANGE IN RMS	
50.0 PCT.	0.0156	* If it is assumed that the errors can only take on the extreme values of the tolerances, the 97.7 percent probable change in RMS is 0.0786
84.1 PCT.	0.0283	
97.7 PCT.	0.0399 *	
99.9 PCT.	0.0505	

-----

## POSITION 1

 PERFORMANCE SUMMARY  
 POLYCHROMATIC RMS WAVEFRONT ABERRATION
 

---

WAVELENGTH	WEIGHT
3950 NM	202
3500 NM	203
2800 NM	176
2000 NM	86
1300 NM	10

---

RELATIVE FIELD	WEIGHT	DESIGN	DESIGN + TOL *	COMPENSATOR RANGE (+/-) *
				DLT S13
0.00, 0.00	1	0.0948	0.1347	0.179287
0.00, 0.30	1	0.108	0.1597	0.179287
0.00, 0.62	1	0.1285	0.2083	0.179287
0.00, 0.70	1	0.136	0.2274	0.179287
0.00, 0.78	1	0.1453	0.2462	0.179287
0.00, 1.00	1	0.1362	0.2552	0.179287

---

\* The probable change and cumulative probability results are based on the assumption that the distribution of the RMS converges to a Gaussian form

The compensator range is a mean plus 2 Sigma value.

Linear compensators are in units of millimeters.

Angular compensators are in radians.

Tolerance coefficients can be saved with the lens to speed up subsequent TOR executions

## References

- Aikens, D., DeGroot, J. E., & Youngworth, R. N. (2008). Specification and Control of Mid-Spatial Frequency Wavefront Errors in Optical Systems. *Optical Fabrication and Testing*. doi:10.1364/OFT.2008.OTuA1
- Fischer, R. E. (1992). What's So Different About IR Lens Design. *Lens Design: Critical Reviews of Optical Science and Technology, CR41*, 117-139.
- Fischer, R. E., Tadic-Galeb, B., & Yoder, P. R. (2008). *Optical System Design* (2nd ed.). New York: McGraw Hill.
- Gat, N., Zhang, J., De Li, M., Chen, L., & Gurrola, H. (2007). Variable Cold Stop for Matching IR Cameras to Multiple f-number Optics. *SPIE Proceedings: Infrared Technology and Applications, XXXIII*, 6542. doi:10.1117/12.720812
- Hasenauer, D. (2015). Optical Design Tolerancing A Key to Product Cost Reduction.
- Hönlinger, B., & Nasse, H. H. (2009). Distortion.
- Parks, R. E. (2008). Specifications: Figure and finish are not enough. *SPIE Proceedings: An Optical Believe It or Not: Key Lessons Learned, 7071*. doi:10.1117/12.798223
- Riedl, M. J. (2001). *Optical Design Fundamentals for Infrared Systems* (2nd ed.). Bellingham, WA: SPIE Press.
- Smith, W. J. (1985). Fundamentals of Establishing an Optical Tolerance Budget. *SPIE Proceedings: Geometrical Optics, 531*, 196-204. doi:10.1117/12.946513
- Synopsys. (2015). Code V 40 Years of Superior Optical Design [Brochure].
- Taylor-Hobson. (2015). PGI Optics [Brochure].
- Weed, K., & Holloway, T. (n.d.). Ensquared and Encircled Energy Testing Attains 'Automated' Status. Retrieved February 02, 2016, from <http://opticalsystems.com/about-us/case-studies/ensquared-and-encircled-energy-testing-attains-automated-status/>